A&A 387, 642–664 (2002)
DOI: 10.1051/0004-6361:20020375

Astronomy & Astrophysics

Oscillations above sunspots: Evidence for propagating waves?

E. O'Shea[1,⋆], K. Muglach[2], and B. Fleck[3]

[1] ESA Research and Scientific Support Department (RSSD), ESTEC, Keplerlaan 1, 2201 AZ, Noordwijk, The Netherlands
e-mail: eoshea@rssd.esa.int

[2] Astrophysikalisches Institut Potsdam, Telegrafenberg, 14482 Potsdam, Germany
e-mail: k.muglach@aip.de

[3] ESA Research and Scientific Support Department (RSSD), NASA/GSFC, Mailcode 682.3, Greenbelt, MD 20771, USA
e-mail: bfleck@esa.nascom.nasa.gov

Received 21 December 2001 / Accepted 8 March 2002

Abstract. We present results of an analysis of time series data observed in sunspot umbral regions. The data were obtained in the context of the SOHO Joint Observing Program (JOP) 97 in September 2000. This JOP included the Coronal Diagnostic Spectrometer (CDS) and the Michelson Doppler Imaging (MDI) instrument, both part of SOHO, the TRACE satellite and various ground based observatories. The data was analysed by using both Fourier and wavelet time series analysis techniques. We find that oscillations are present in the umbra at all temperatures investigated, from the temperature minimum as measured by TRACE 1700 Å up to the upper corona as measured by CDS Fe XVI 335 Å ($\log T = 6.4$ K). Oscillations are found to be present with frequencies in the range of 5.4 mHz (185 s) to 8.9 mHz (112 s). Using the techniques of cross-spectral analysis time delays were found between low and high temperature emission suggesting the possibility of both upward and downward wave propagation. It is found that there is typically a good correlation between the oscillations measured at the different emission temperatures, once the time delays are taken into account. We find umbral oscillations both inside and outside of sunspot plume locations which indicates that umbral oscillations can be present irrespective of the presence of these sunspot plumes. We find that a number of oscillation frequencies can exist co-spatially and simultaneously i.e. for one pixel location three different frequencies at 5.40, 7.65 and 8.85 mHz were measured. We investigate the variation of the relative amplitudes of oscillation with temperature and find that there is a tendency for the amplitudes to reach a maximum at the temperature of O III (and less typically O V and Mg IX) and then to decrease to reach a minimum at the temperature of Mg X ($\log T = 6.0$ K), before increasing again at the temperature of Fe XVI. We discuss a number of possible theoretical scenarios that might explain these results. From a measurement of propagation speeds we suggest that the oscillations we observe are due to slow magnetoacoustic waves propagating up along the magnetic field lines.

Key words. Sun: sunspot – Sun: oscillations – waves

1. Introduction

It has been known for more than thirty years that oscillations are present in the chromosphere above sunspot umbra (see review by Lites 1992 and references therein). The dominant frequency of these chromospheric umbral oscillations, measured in both Doppler shifts and intensity fluctuations, is typically around 5.5 mHz (i.e. three min) with no significant power peaks present in the 5-min band (see e.g. Lites 1986b; Thomas et al. 1987). Oscillations in the higher temperature transition region above sunspot umbra were first observed by Gurman et al. (1982) using the UVSP instrument on the Solar Maximum Mission (SMM). They observed oscillations in both velocity and intensity with frequencies in the 5.8–7.8 mHz range using the C IV 1548 Å resonance line. Using similar observations with the same C IV line from the UVSP instrument together with ground based observations of the photospheric Fe I line and the chromospheric lines of Ca II and He I Thomas et al. (1987) were the first to obtain simultaneous measurements of oscillations at different heights above the umbra. They found that there were two main oscillation modes in these lines, one at 5.5 mHz and another at 7.5 mHz. From cross-coherence measurements the mode at

Send offprint requests to: E. O'Shea,
e-mail: eoshea@ll.iac.es

⋆ *Present address*: Instituto de Astrofisica de Canarias (IAC), C/ Via Láctea s/n, 38200 La Laguna, Tenerife, The Canary Islands, Spain, e-mail: eoshea@ll.iac.es

Table 1. Details of the CDS temporal series observations.

Date	Datasets	Sequence	Pointing X, Y	Start UT	End UT
23 Sep.	s20640r01	GENE	−121, 63	07:26	08:03
23 Sep.	s20641r01	OS_AR	−121, 62	09:10	10:17
26 Sep.	s20679r01	GENE	386, 49	10:48	11:25
26 Sep.	s20680r00	OS_AR	488, 64	12:01	13:07
26 Sep.	s20680r01	OS_AR	488, 64	13:07	14:14

5.5 mHz was found to be coherent between the chromosphere and the transition region (i.e. present in the Ca II, He I and C IV lines) while the oscillation at 7.5 mHz was coherent between the photosphere and the transition region (i.e. in Fe I and C IV but not Ca II or He I), suggesting oscillations with low amplitudes at this frequency in the chromosphere. They proposed that these low amplitudes indicated the presence of a node in the chromosphere.

Recently, with the launch of the Solar and Heliospheric Observatory (SOHO) there has been a renewed interest in this subject with a number of papers published showing evidence for 3 min oscillations in chromospheric and transition region lines in sunspot umbra (Brynildsen et al. 1999a, 1999b, 2000; Maltby et al. 1999, 2001; Fludra 1999, 2001). Fludra (2001) concludes that the three minute umbral oscillations can occur both in so-called sunspot plumes, bright features seen at transition regions temperatures between $1.5-4 \times 10^5$ K above sunspots, and in lower intensity plasma closely adjacent to the plumes. He finds a spread of periods between 120–210 s (i.e. 4.76–8.33 mHz) in the umbra oscillations investigated by him, with power concentrated around periods 160–180 s (i.e. 5.55−6.25 mHz). However, Maltby et al. (2001) show that these three minute oscillations in and near the sunspot plume only occur if the plume is located over a sunspot umbral region.

Brynildsen et al. (1999b, 2000) found that there were measurable time delays of 25 and 31 s respectively between the intensity oscillations in the N V and O V transition region lines and the chromospheric Si II line (for a 172 s period), indicating the upward travel time of a wave from the lower to higher temperature regions. Maltby et al. (1999) have shown tentative evidence that umbral oscillations also extend up to the low corona as measured by the 171 Å channel on the Transition Region and Coronal Explorer (TRACE) satellite.

Based on linear theory two different mechanisms have been discussed to explain the observed 3-min oscillations in the sunspot umbra, one a cavity for fast magnetoacoustic waves in the photosphere and the other a cavity for slow magnetoacoustic waves in the chromosphere (see reviews by Thomas & Weiss 1992 and Lites 1992). Both theories allow for the possibility of leakage (tunnelling) from the cavities so that waves may propagate upwards along the field lines. Gurman & Leibacher (1984) model the 3-min oscillations as upwardly propagating acoustic (i.e. slow-mode) waves that are partially reflected by the steep temperature gradient. Lites (1986a) cites strong evidence in favour of the fast magnetoacoustic wave mechanism. However, it is not clear which of these models is more correct as features exclusive to each are present in observations, e.g. the fast magnetoacoustic mechanism is needed to explain the isolated peaks seen in photospheric power spectra which are correlated with oscillations in the chromosphere yet the slow magnetoacoustic mechanism is perhaps needed to explain the broad spectrum of power above 5 mHz in the chromosphere (Lites 1992).

Recently, Brynildsen et al. (1999a) found evidence for linear upwardly propagating acoustic waves with no evidence for shocks using O V and N V lines from SUMER. The oscillations with periods between 129–173 s described by Gurman et al. (1982) for the C IV line were discussed by Žugžda et al. (1984) in terms of their chromospheric cavity model. In their observations with the same C IV line from the UVSP instrument Thomas et al. (1987) also found no evidence of nonlinearity.

However, other authors have found evidence of nonlinearity in sunspot oscillations. Lites (1986b) found that some oscillations in the umbral chromosphere showed evidence of nonlinearity (suggesting the presence of shocks), i.e. the velocities measured by the chromospheric He I showed the "sawtooth" shape characteristic of nonlinear behaviour. More recently, using data from the SUMER instrument on the Solar and Heliospheric Observatory (SOHO), Brynildsen et al. (1999b) found that oscillations in line-of-sight velocities measured from the transition region lines of O V and N V showed the characteristic nonlinear sawtooth shape while those in the chromospheric Si II did not. They present evidence (using phase and phase difference measurements) to show that these oscillations signify upwardly propagating non-linear (shock) acoustic waves from the chromosphere to the transition region. The obvious presence of non-linear waves in umbral oscillations led Lites (1992) to argue that the eigenmode analyses based on linear models may no longer be viable and that theoretical models that incorporate nonlinear effects (e.g. Carlsson & Stein 1997) offer the best way to make progress.

In this paper we will examine the oscillations present in the umbra above a sunspot using lines covering a range of temperatures from the low chromosphere to the corona. By using simultaneous observations over this temperature range we hope to find a connection between oscillations in the chromosphere, transition region and corona which may indicate the presence of propagating waves.

2. Observations and data reduction

The data used in this work were obtained in the context of a Joint Observing Program or JOP that was run between 19–29 September 2000 in a number of active regions on the Sun. This JOP was a coordinated observing campaign which included the Coronal Diagnostic Spectrometer (CDS) (Harrison et al. 1995), the Michelson Doppler Imager (MDI) (Scherrer et al. 1995), both part

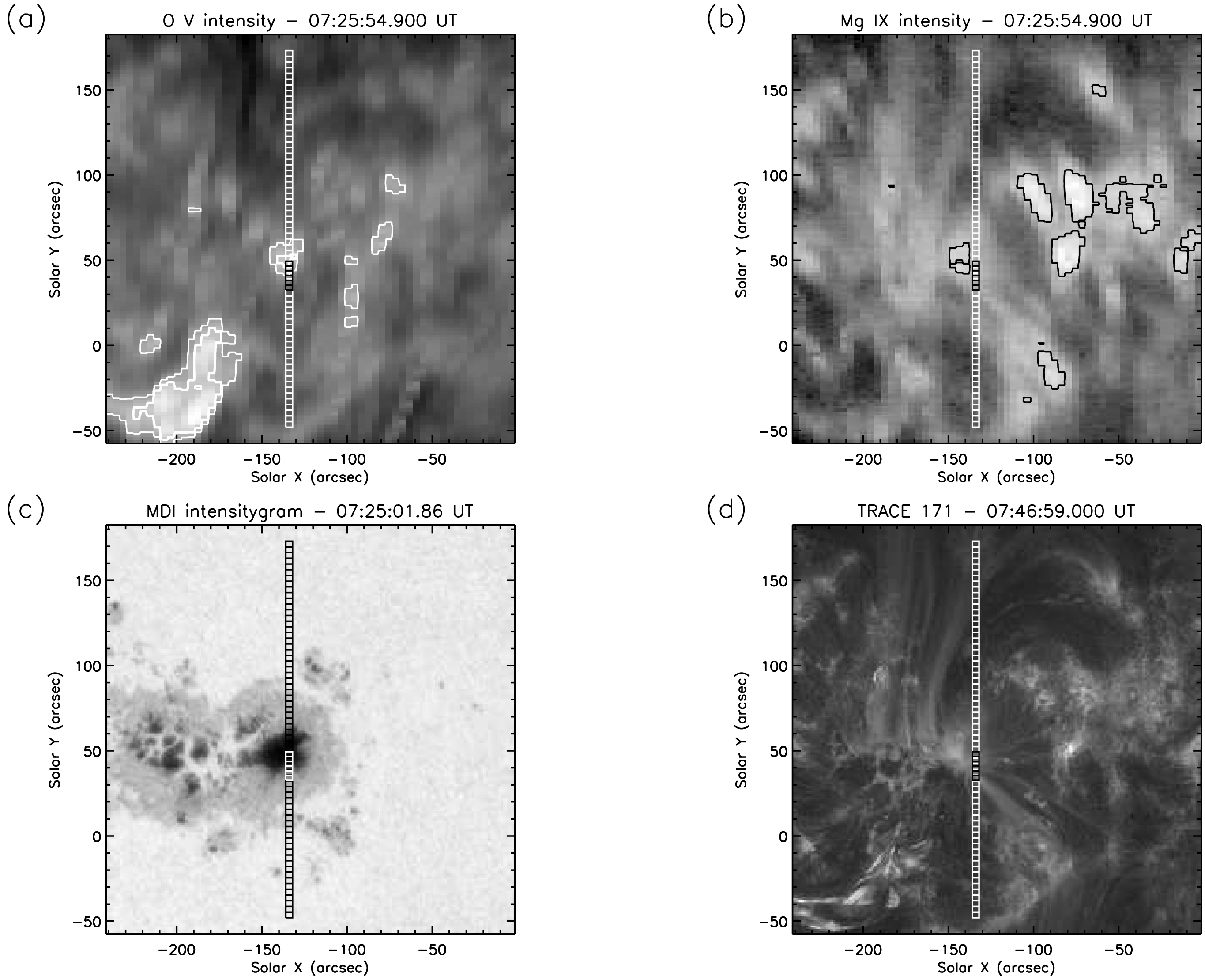

Fig. 1. a) CDS raster image in O V ($\log T = 5.36$ K). The overplotted white rectangle is the starting location of the slit for the s20640r01 dataset. The thin white contours show the locations where the intesity $I \geq 2.5\,\bar{I}$ while the thicker contours show the locations where $I \geq 5\,\bar{I}$. **b)** CDS raster image of Mg IX ($\log T = 6.00$ K). The black contours show the location of intensity where $I \geq 2.5\,\bar{I}$ **c)** MDI intensitygram showing the location of the slit relative to the sunspot umbra and penumbra. **d)** TRACE 171 image of the sunspot area. In these images pixels number 24–29 have been highlighted with either white or black boxes.

of the Solar and Heliospheric Observatory (SOHO), the Transition Region and Coronal Explorer (TRACE) satellite (Handy et al. 1999) and various ground based observatories (GBOs). We shall not discuss the ground based observations in this work but more details on the full JOP (No. 97 in the SOHO designation) may be found in the SCIENCE: Operations section of the SOHO webpage (`http://sohowww.nascom.nasa.gov/`).

The CDS time series observations presented here were obtained on the 23 and 26 September 2000 in sunspot umbra regions associated with AR 9169. Details of the observations including pointing and start times are shown in Table 1. Two different CDS sequences were run to obtain these observations, OS_AR and GENE, both of which used the Normal Incidence Spectrometer (NIS) of the CDS instrument.

For the OS_AR sequence, a temporal series observation, 200 time frames each with a cadence of ∼20 s were obtained using the 4×240 arcsec^2 slit. For these observations the slit was windowed so that only 222 arcsecs of the slit length were used. For the NIS detector of CDS the pixels in the y direction (i.e. the spatial resolution) are of size 1.68 arcsecs. For these observations we used an onboard binning of two in the y direction so that the new pixel size in the y direction was 3.36 arcsec. Within the 222 arcsec length of the slit there are therefore 66 different pixels of size 4×3.36 arcsec^2. The OS_AR sequence contains the lines of He I 584.3 Å ($\log T = 4.55$), O III 599.6 Å ($\log T = 5.01$), O V 629.7 Å ($\log T = 5.36$), Mg IX 368.1 Å ($\log T = 6.00$), Mg X 624.9 Å ($\log T = 6.10$) and Fe XVI 335.4 Å ($\log T = 6.40$). (The temperatures quoted here are the formation temperatures of the lines and were calculated using the equation $T^{-1/2}\exp(\Delta E/kT)A$, where ΔE is the excitation energy of the transition and A is the relative ion abundance taken from Mazzotta et al. 1998.)

In the GENE sequences the 4×240 arcsec^2 slit was moved 60 times in steps of 4 arcsec so as to build up 240×240 arcsec^2 raster images. For the GENE sequence the lines used were He I 584.3 Å ($\log T = 4.55$), O III 599.6 Å ($\log T = 5.01$), O V 629.7 Å ($\log T = 5.36$), Mg IX 368.1 Å ($\log T = 6.00$), Mg X 624.9 Å ($\log T = 6.10$), Si XII 520.7 Å ($\log T = 6.30$) and Fe XVI 335.4 Å ($\log T = 6.40$). These raster images were used for coalignment of CDS with TRACE to ensure that oscillations measured from both instruments originated from the same umbral location.

We note that all these observations were obtained after the recovery of SOHO (end of 1998) and so the lines show the characteristic broadened wings. This broadening has the effect of blending the Mg IX 368 Å line with that of the nearby Mg VII 367 Å line. We were able to fit the Mg IX component of this blend satisfactorily by using a double Gaussian, and by fixing the position of the Mg VII line. In all other cases fitting was done using a single Gaussian as the lines were found to be generally symmetric. We subsequently obtained the total number of photon-events in a line by integrating under the fitted line profile.

The CDS data was calibrated (flat-fielding, debiasing etc.) using the standard software routines of which full details are given in the paper by O'Shea et al. (2001). We note that rotational compensation was not used for any of the temporal series datasets in OS_AR and the data was thus obtained in a sit-and-stare mode. Due to the relatively large width of the slit (4 arcsec), and following the discussion of Doyle et al. (1998) for Fourier power spectra, we estimate that the effect of the sit-and-stare mode on the resulting (Fourier/wavelet) power, for all datasets examined, would be to spread the power over a frequency range of *at most* $\sim$1 mHz, depending on the size of the source.

TRACE data were obtained on the 23 and 26 September 2000 in the same sunspot umbra regions associated with AR 9169 in the three passbands of 1550, 1600 and 1700. Temporal series data were obtained using these three filters between the times of 8.00 and 12.00 UT on both days. However, on the 26 September the data from the CDS and TRACE instruments were not obtained simultaneously, the TRACE observations having ended at 12:00 UT before the CDS observations had begun, and thus the time series from the two instruments on this day cannot be directly compared. For the data obtained on the 23 September 403 images of size 512×512 arcsec^2 were obtained over this four hour period, with a resulting cadence of 22 s.

Before the TRACE data could be used it had to first be calibrated. The TRACE data was firstly corrected for a dark offset and normalized to exposure time (thus giving data-numbers/s). Due to its highly inclined near Earth orbit the spacecraft moves regularly through the Earth's radiation belts. The contamination of the images by high energetic particles has been removed by using a despike routine. Missing images were filled in by linear interpolation of neighbouring images. No pixel-to-pixel flatfielding is currently available for the data. Nevertheless, the large–scale decrease of sensitivity in the centre of the CCD has been taken into account. As the CDS data was obtained in a "sit-and-stare" mode (i.e. with no compensation for solar rotation) we do not apply solar rotation correction to the TRACE images. An additional image drift is in the range of a few pixels over the orbit of the TRACE spacecraft. This has been calculated using cross-correlation methods and is removed from the data. A more detailed description of the full TRACE data reduction can be found in Muglach (2002).

The emission from the 1700 passband is estimated to come from the temperature minimum region of the Sun's atmosphere (Judge et al. 2001; Handy et al. 1999). The emission contained in the 1550 and 1600 passbands is less easy to categorise due to the presence of significant contributions from C IV lines at 1548 and 1550 Å and from neighbouring continuum and lines. Handy et al. (1999) point out that an image obtained from these passbands is neither a pure "C IV" image nor a pure "UV continuum" image but something of a mix of the two. However, they further mention that images in these bandpasses resemble images taken in the centre of the Ca II K line with a bandpass of a few Angstroms. Therefore it seems likely that the majority of the emission in the 1550 and 1600 passbands comes from the lower atmosphere of the Sun, e.g. the low chromosphere. In fact, from Vernazza et al. (1981) the 1550 Å radiation might be expected to come from the lower chromosphere while the 1600 Å would be expected to come from just above the temperature minimum region. So of the three TRACE passbands, 1550, 1600 and 1700, we suggest that the 1700 passband emission is formed at the lowest height in the atmosphere, followed in height by the 1600 and 1550 passbands respectively.

In addition to the three UV passbands data was also taken in the TRACE 171 and 5000 (white light) passbands either before or after the other observations in order to provide context images. The size of these images are typically either of size 768×768 or 1024×1024 arcsecs^2.

In order to directly compare the time series obtained from CDS and TRACE instruments for the 23 September it was first necessary to coalign the CDS and the TRACE data. To do this we used a method of 2-D cross-correlation of the TRACE images and the CDS raster images obtained from the GENE sequence. It was found that emission measured in the lowest temperature CDS raster of O III ($\log T = 5.01$) was sufficiently similar in structure to that measured in the TRACE 1700 image for a successful cross-correlation to be carried out. The results from the cross-correlation give us the amounts in arcsec by which to shift the TRACE images so that they are exactly coaligned withthe CDS raster. The errors of this cross-correlation technique are estimated to be no more than $\sim$2 arcsec at worst. As the 4×222 arcsec^2 slit coordinates for the CDS time series observations (from sequence OS_AR) are

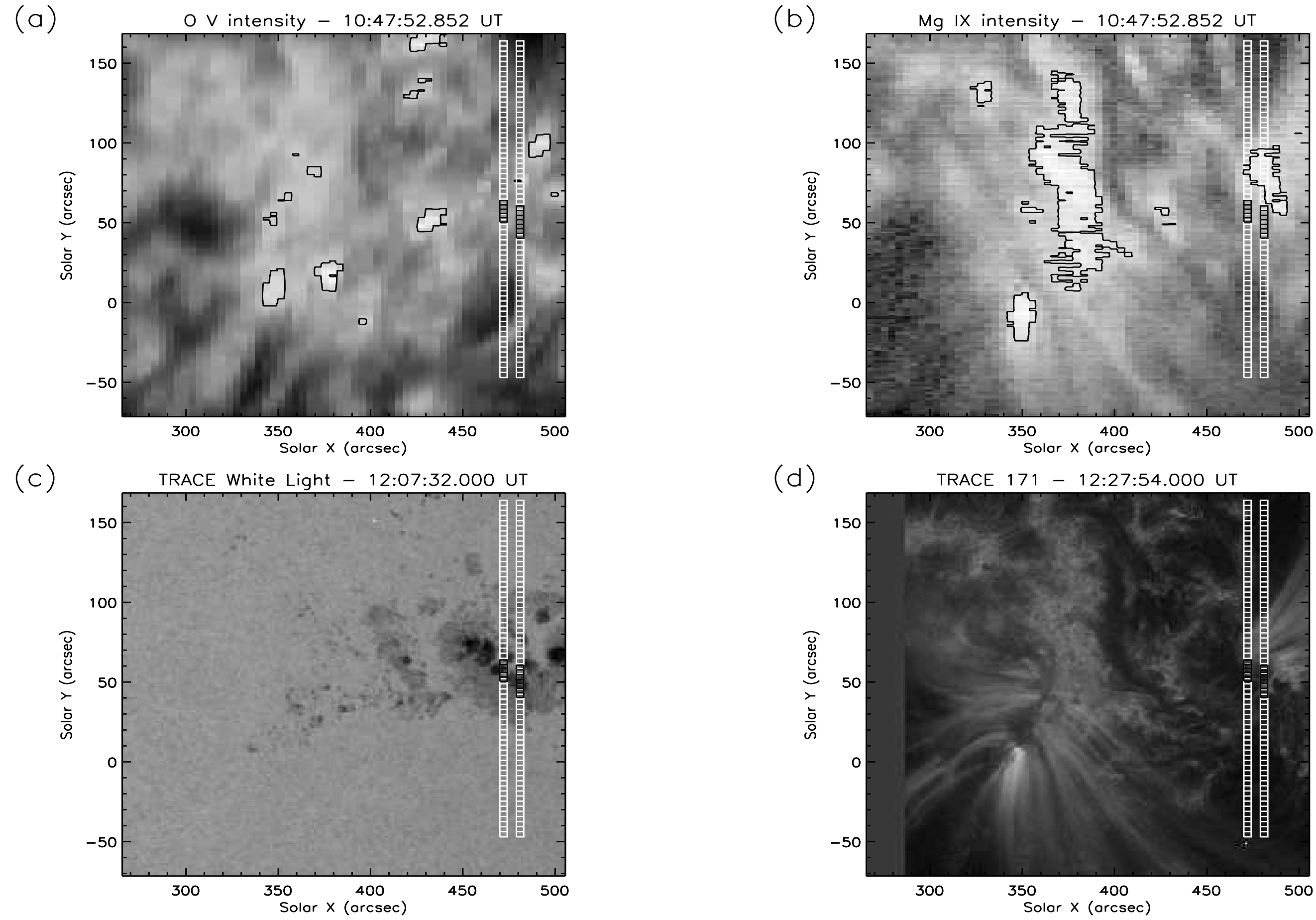

Fig. 2. a) CDS raster image in O v ($\log T = 5.36$ K). The overplotted white rectangle is the starting location of the slit for the s20680r00 (right) and s20680r01 (left) datasets (Note that only the first 63 pixels of the slit are plotted here). The thin black contours show the locations where the intesity $I \geq 2.5\,\bar{I}$. **b)** CDS raster image of Mg IX ($\log T = 6.00$ K). The black contours show the location of intensity where $I \geq 2.5\,\bar{I}$ **c)** TRACE white light image showing the location of the slit relative to the sunspot umbra and penumbra. **d)** TRACE 171 image of the sunspot area (the first 20 arcsec in the X direction is left blank due to a lack of data in this region). In these images pixels number 26–32 for s20680r00 and 29–33 for s20680r01 have been highlighted with black boxes.

known accurately relative to the coordinates of the CDS raster images we were then able to map the equivalent location of the CDS time series slit of size 4×222 arcsec^2 onto the resulting coaligned TRACE images. As the spatial resolution of the TRACE images is 0.5 arcsec/pixel it was necessary to sum over 8 pixels in the X direction and 7 pixels in the Y direction to approximate the size of a CDS pixel of size 4×3.36 arcsec^2. By doing this it was possible to produce artificial TRACE "pixels", of the same size as the CDS pixels containing emission over the same areas of the sunspot as the CDS pixels. We note that it is not sufficient to use the pointings in the headers of the CDS and TRACE datasets in order to do the coalignment as it was found by the authors that this will result in errors of approximately 10–15 arcsecs in the resulting X and Y coordinates. As we have mentioned earlier the cadence of the CDS time series is $\sim$20 s while that of the TRACE time series is $\sim$22 s. In order to directly compare the results from the time series of both instruments it was first necessary to interpolate each time series to a new common "cadence" of 1 s, which is also then the new temporal resolution of this data.

On the 23 September magnetograms, intensitygrams and Dopplergrams were also obtained in the same active region AR 9169 with MDI being operated in its high resolution (HR) mode. The cadence of the observations was 60 seconds and the field-of-view $\sim$$425 \times 425$ arcsec^2, i.e. 700×700 pixels. In this work we shall not examine the MDI time series datasets obtained on 23 September. This is because there were unfortunately found to be no suitable complete time series available at the same times as the CDS observations. This was also true for the CDS data obtained on the 26 September, where only full-disk MDI intensitygrams/magnetograms are available. For the 23 September data we use one of the HR MDI intensitygram images as a context image in order to accurately determine the location of the CDS time series slit in the sunspot umbra and penumbra. First we co-aligned the CDS O III raster and the TRACE 1700 image of this date, again using a 2-D cross-correlation in order to get the location of the CDS time series slit in relation to the TRACE image. Then by co-aligning this same TRACE 1700 image with the MDI intensitygram we were able to estimate the location of the CDS time series slit in the MDI intensitygram image by their common relationship to the TRACE image. We note that we were not able to directly cross-correlate the CDS O III raster and MDI intensitygram as the structure of their respective emission was too different.

3. Results

3.1. Location of the oscillations

In Figs. 1a and b we show CDS intensity rasters of size 240 × 240 arcsec^2 for the transition region line of O V ($\log T = 5.36$ K) and the coronal line of Mg IX ($\log T = 6.0$ K). These rasters were obtained from dataset s20640r01, the details of which are described in Sect. 2 and in Table 1. These raster images show part of the large active region AR 9169 observed on 23 Sep. 2000. In Figs. 1c and d we show the same region using a high resolution MDI intensitygram and a TRACE 171 passband image. Note that the intensities plotted in Figs. 1a, b and d are the logarithms of the original intensities, done to highlight the lower intensity regions for comparison purposes. The times at which each image was obtained are shown in the image titles. The rectangle overplotted on these images is the starting location of the 4 × 222 arcsec^2 slit for the time series dataset s20641r01, obtained as part of the OS_AR sequence (see last section). The slit rectangle has been divided into 66 boxes, each representing the individual CDS pixels of size 4 × 3.36 arcsec^2. Looking at the O V intensity raster first (Fig. 1a) it is noticeable that there are a number of regions that show enhanced brightenings. These regions are marked by white contours in this plot. The thin line contours represent $I \geq 2.5\,\bar{I}$ and the thicker contours represent $I \geq 5\,\bar{I}$, where $\bar{I}$ denotes the average intensity over the whole 240×240 arcsec^2 area. We choose these contour thresholds following the definitions of Maltby et al. (1999) and Brynildsen et al. (1999c) concerning sunspot plume indentifications. We note that the slit passes through one of these bright regions ($\geq 5\,\bar{I}$) at coordinates $X = -134$, $Y = 50$, which also corresponds to the location of an umbral region in the MDI intensitygram in Fig. 1c. By the definition of Maltby et al. this is therefore the location of a sunspot plume. In Fig. 1b for the Mg IX raster the $I \geq 2.5\,\bar{I}$ contours have been marked by thin black lines; there are no brightenings of $I \geq 5\,\bar{I}$ in this raster. We note that the slit does not pass through any of these brighter regions but that there is a bright area marked by contours just to the left of the slit at approximate coordinates $X = 145$, $Y = 50$. Over the course of the ∼66 min duration of the s20640r01 time series dataset the Sun will rotate by ∼10 arcsec and thus will bring this bright area into our observing slit. As this bright area in the Mg IX raster also occurs in the vicinity of the sunspot umbra (see Fig. 1c) we can also reasonably describe it as a sunspot plume. By comparing the Mg IX raster with that of the TRACE 171 image in Fig. 1d we can see that they share the same general structure, taking the differences in resolution into account. This would appear to indicate that the emission in the TRACE 171 filter is predominately at the same temperature as the Mg IX line, i.e. at $\log T = 6.0$ K. The brightening discussed in the Mg IX raster at coordinates $X = 145$, $Y = 50$ is present at the same coordinates in the TRACE 171 image. We can also see by comparing the CDS Mg IX and TRACE 171 images that many of the bright structures in the CDS raster image are due to complex loop structures, in particular the network of loops to the left of the bright area already discussed, that end in the sunspot but which originate at some distance from the sunspot.

In Fig. 2 we show the equivalent images for the data taken in AR 9169 on the 26 Sep. 2000. Here the overplotted white boxes are the starting 4 × 240 arcsec^2 slit locations of the s20680r00 and s20680r01 time series datasets. However, note that the slit plotted is only the first 63 pixels, the top three pixels from 64–66, are not plotted here as they do not fit in the field-of-view of the raster images. The s20680r01 slit is plotted to the left of the s20680r00 slit indicating its later start-time. In both the O V and Mg IX images the black contours shown are those of $I \geq 2.5\,\bar{I}$ brightenings; no brightenings of $I \geq 5\,\bar{I}$ are present. In Fig. 2c we show a TRACE white light image. It will be noticed that the slits from the two datasets pass through a number of small umbral regions. In fact, these small umbral regions are the same ones seen earlier at approximate coordinates of $X = (-190)-(-210)$, $Y = 20-70$ in the MDI intensitygram of 23 Sep. and shown in Fig. 1c. By comparing the O V raster image in Fig. 2a and the TRACE white light image in Fig. 2c it is clear that the location of these small umbral regions does not correspond to any $I \geq 5\,\bar{I}$ or $I \geq 2.5\,\bar{I}$ brightenings in O V. Thus we can conclude that there is no sunspot plume here at the temperature of O V. The situation as regards the Mg IX is slightly different in that the two slits pass through a brightening at $Y \approx 55-95$ which, by comparison with the TRACE white light image, is the location of a number of small umbral regions. It is likely that this is a weak plume similar to that seen in Fig. 2b which was also visible in the Mg IX line. In Fig. 2d we plot the TRACE 171 image. Again the similarities in general structure with the Mg IX raster image are obvious, highlighting their similar formation temperatures. By comparing the location of the weak Mg IX plume feature with the TRACE 171 image it can be seen that the weak Mg IX plume overlies the footpoints of arching loop structures.

In Fig. 3 we show the results of a wavelet analysis of O V for a single pixel, No. 28, along the slit for dataset s20641r01. This is one of the pixels from 24–29 that were highlighted in the images in Fig. 1. This pixel therefore is within the sunspot plume discussed in Fig. 1. We use a similar wavelet analysis as outlined in O'Shea (2001), with the original software having come from Torrence & Compo (1998). In the time series shown in the top panel of Fig. 3, a strong oscillation signature is clearly present between ∼15–40 min. From the wavelet spectrum, shown in

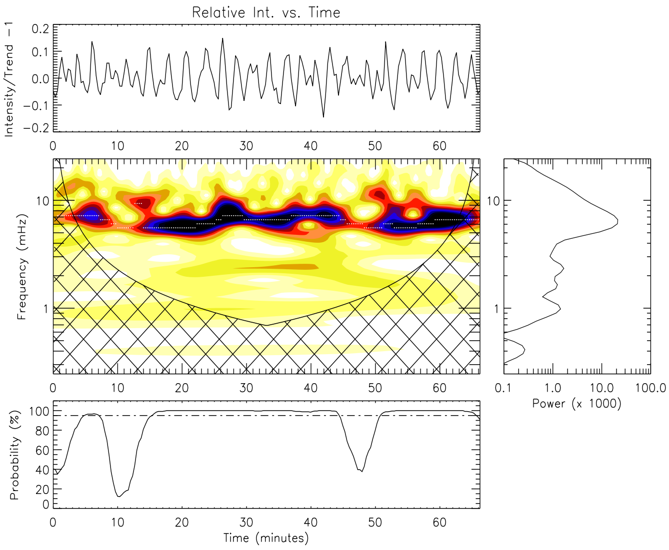

Fig. 3. The intensity time series (top panel), wavelet power spectrum (middle left), averaged wavelet (global) spectrum (middle right panel) and (bottom panel) the variation of the probability with time from the randomisation test for the O V line in pixel 28 of time series dataset s20641r01. In the bottom panel the dot-dashed line shows the 95% significance level. Note that for the wavelet power spectrum the colour table has been reversed, so that the highest powers are plotted as the darkest shades.

the middle panel, the frequency of this oscillation is measured to be at ∼5–7 mHz, with slight variations between these values occurring over the length of the observation time. Note that the wavelet spectrum plot has a reversed colour table so that the highest powers are plotted as the darkest shades. The maximum power peak in the global wavelet plot (i.e. the average of the wavelet spectrum over time) occurs at a frequency of 6.6 mHz. The wavelet analysis has been carried out on relative intensity and hence there is a lack of low frequency power in the wavelet spectrum plot. The relative intensity was calculated by using a similar technique to that outlined in Fludra (2001), i.e. the trend of the time series was first calculated by using a 30 point running average, the original time series was then divided by the trend and a value of 1 subtracted from the result. It was found this method was efficient at removing low frequency background oscillations. In the lowest panel in Fig. 3 we plot the variation of the probability, estimated from a randomisation test (see O'Shea et al. 2001), which gives an estimate of the statistical significance of the power at each time. Probabilities greater than 95% are considered significant and from this plot it is clear that the oscillations discussed here are statistically significant over most of the observing time. Note that the statistical significance is calculated only for the maximum powers in the wavelet spectrum marked by the thin white line. The maximum power in the global wavelet spectrum was also similarly found to be significant with a probability of greater than 95%.

From this one pixel located in the sunspot plume we have thus found that the average frequency of oscillation

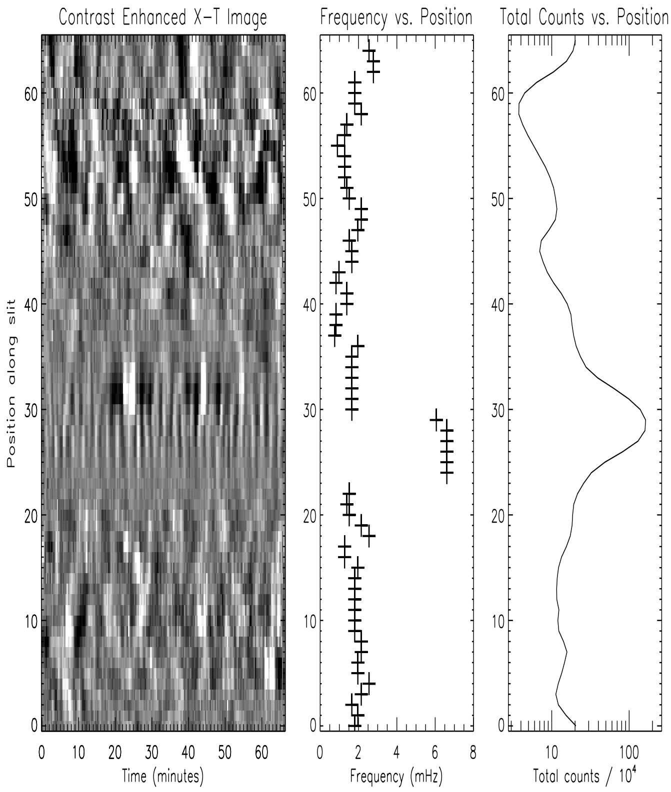

Fig. 4. (left panel) Contrast enhanced O V intensity map (X-T image) of the variation of intensity along the slit versus time, (middle panel) variation of the frequency versus pixel position and (right panel) the summed counts over time at each pixel position for dataset s20641r01. The grey scale coding has the most intense regions as white in the intensity map.

over the whole observation time for the O V line is 6.6 mHz (152 s), as estimated from the global wavelet spectrum. In order to show the spatial variation in oscillation frequency over the whole slit we plot in Fig. 4 a contrast enhanced X-T image, the frequencies measured from the global wavelet spectrum for each of the 66 (0–65) pixel positions along the slit and the summed total of counts over time for each of these 66 pixel positions. The X-T image was contrast-enhanced by removing the low frequency trend of the oscillations (i.e. by calculating the relative intensity) for each of the positions along the slit. In the X-T image large areas of brightenings and darkenings, representing longer period oscillations, are present from pixel positions 0–20 and from 40–65, which, by comparison with Fig. 1c, represent the portion of the slit outside of the sunspot penumbra and umbra. That portion of the slit inside the sunspot, from roughly 20–40 pixels can be seen to contain many light and dark ridges from approximately pixels 24–33, i.e. from those pixels approximately inside the umbra. These light and dark ridges represent oscillations of 5–7 mHz, as we have seen in Fig. 3 for one of them, pixel 28. It is noticeable that those pixels representing penumbral oscillations, i.e. from 20–24 and from 33–40, do not show any bright and dark intensity variations or ridges indicating that strong oscillations are not common in the penumbral region. Looking at the plot of frequency versus position (central panel) it can be seen that most of the pixels along the whole slit have oscillation frequencies between ∼0.5–2.5 mHz, except for the small number of pixels between 24–29 which show higher frequencies of 6–6.6 mHz. The pixels from 24–29 are those six pixels that were highlighted in the slits overplotted on the images in Fig. 1. These pixels are from the range of pixels from 24–33 that was shown in the X-T image to contain light and dark ridges. However, the pixels from 30–33 in this range do not show an average frequency of 6–6.6 mHz due to the presence of small flaring events at times between ∼20–30 and 40–50 min that interfere with the measurement of the underlying higher frequency oscillations. If we examine Fig. 1c more closely we can see that the pixels from 24–29 are mostly present in the umbra region of the sunspot, except for pixels 24 and 25 that represent oscillations coming from the penumbra region. However, this may be an effect of the different heights of formation of the emission in each case, i.e. the O v emission is formed at a much heigher temperature and hence height than the photospheric emission in the MDI intensitygram and thus we might not expect it to exactly overlie it due to the opening out of flux tubes and other possible spatial movements with height in the atmosphere. Hence we can reasonably assume that all the oscillations with frequencies between 6–6.6 mHz originate from the umbra. Indeed in a recent paper Maltby et al. (2001) show that when oscillations occur in a plume, the plume is always present over a sunspot umbra. If we examine these six pixels from 24–29 in Fig. 1a it is apparent that only the top two or three pixels are within the sunspot plume of O v. However, we note that pixels 30–33, if they were not affected by the small flaring events, would also represent higher frequency oscillations in the sunspot plume.

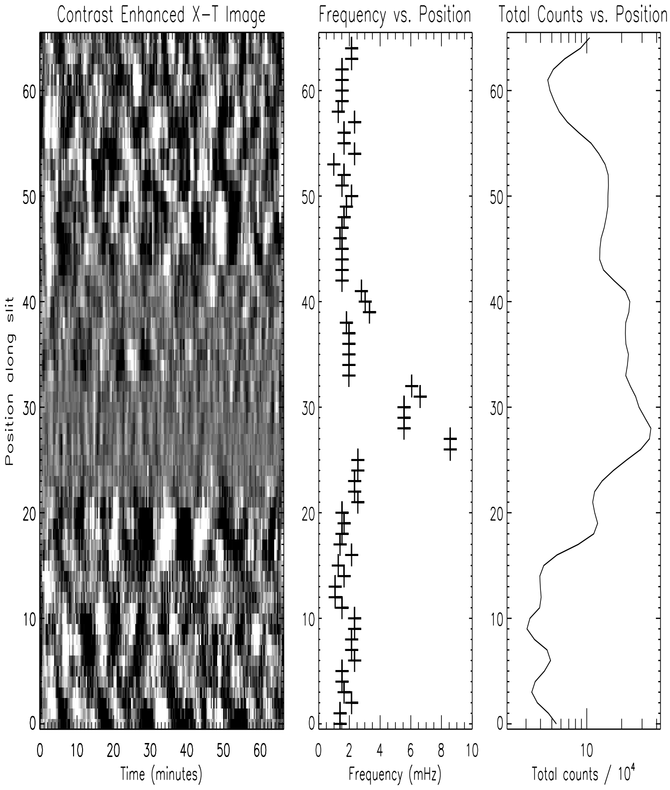

Fig. 5. (left panel) Contrast enhanced O v intensity map (X-T image) of the variation of intensity along the slit versus time, (middle panel) variation of the frequency versus pixel position and (right panel) the summed counts over time at each pixel position for dataset s20680r00. The grey scale coding has the most intense regions as white in the intensity map.

In Figs. 5 and 6 we carry out a similar analysis for datasets s20680r00 and s20680r01, respectively. In Fig. 5 it is possible to see the faint light and dark ridges in the X-T image, signatures of the oscillations, between pixel numbers 26–32. Similarly these ridges may also be seen between pixels 29–33 in Fig. 5 for dataset s20680r01. These light and dark ridges correspond to oscillations at these locations. If we look at the plots of frequency versus position in the middle panels of these plots we can again see that at certain locations along the slit, from 26–32 pixels in the case of s20680r00 and from 29–33 in the case of s20680r01, there are pixels with high frequency values of between ∼6–8 mHz. These are the pixels that were highlighted in the slits overplotted in Fig. 2. From Fig. 2c, the TRACE white light image, it is possible to see that these highlighted pixels from both datasets occur in a region of the sunspot that contains a number of small umbral regions. Moreover, the highlighted pixels from 26–32 and from 29–33 occur in the footpoints of arching loop structures as discussed in the previous subsection. This can be confirmed by looking at Fig. 2d. It is noticeable, after comparing with the plots of total counts versus position in the righthand panels of Figs. 5 and 6, that the oscillations between 26–32 in s20680r00 and 29–33 in s20680r01 are not coming from particularly bright regions of O v emission relative to the rest of the slit locations. In addition, by comparing the TRACE white light image in Fig. 2c with the CDS raster images of Figs. 2a and b it is clear that these highlighted pixels, and hence the higher frequency oscillations that occur in these pixels, are not present as part of any sunspot plume, as no plumes exist at their location (as discussed in Sect. 3.1).

In Fig. 7 we show the results of a wavelet analysis in O v for pixel 27 in dataset s20680r00. From Fig. 2c this can be seen to be one of the pixels that contains emission from a small umbral region. From the plot of the time series in the top panel it is clear that the main oscillations take place during the first half of the observation time. However, it is possible to see from the wavelet spectrum that during this 30 min at the start of the observation that the oscillation frequency changes abruptly from a value of ∼8.5 mHz for the first 20 min to a value of ∼5.5 mHz for the rest of the observation time. That is, there are two distinct and different oscillation frequencies occurring within the observation time. This is possibly due to different sunspot elements rotating in and out of the field-of-view of the CDS slit during the course of the observations. From the randomisation test in the lower most panel it can be seen that these oscillations are significant, above

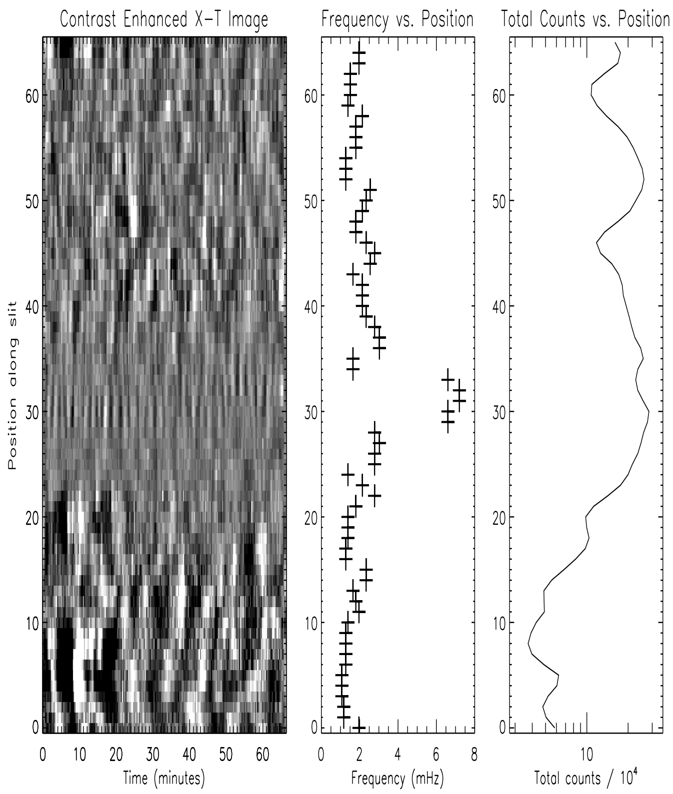

Fig. 6. (left panel) Contrast enhanced O v intensity map (X-T image) of the variation of intensity along the slit versus time, (middle panel) variation of the frequency versus pixel position and (right panel) the summed counts over time at each pixel position for dataset s20680r01. The grey scale coding has the most intense regions as white in the intensity map.

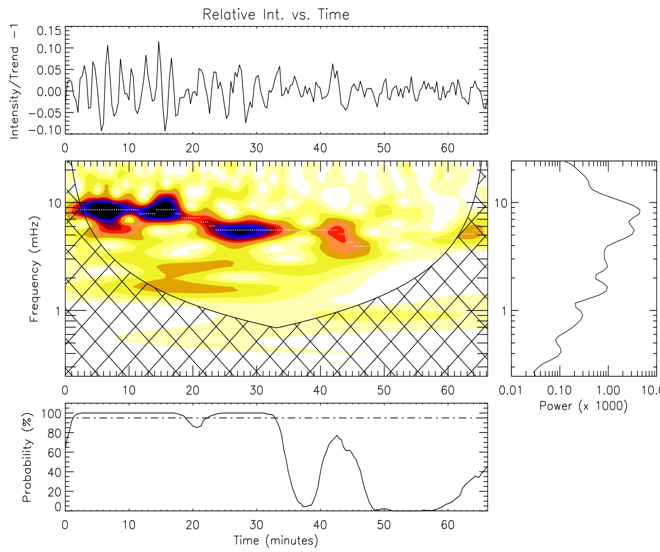

Fig. 7. The intensity time series (top panel), wavelet power spectrum (middle left), averaged wavelet (global) spectrum (middle right panel) and (bottom panel) the variation of the probability with time from the randomisation test for the O v line in pixel 27 of time series dataset s20680r00. In the bottom panel the dot-dashed line shows the 95% significance level. Note that for the wavelet power spectrum the colour table has been reversed, so that the highest powers are plotted as the darkest shades.

the 95% significance level, for most of the first 35 min of the observation. Note, as before in Fig. 3, that the statistical significance is calculated only for the maximum powers in the wavelet spectrum marked by the thin white line. Similar results were found for other pixels in the range 26–29 for dataset s20680r00. However, for pixels 30–32 the oscillations change, with the main oscillations now occurring towards the end of the observation time. This would indicate that a new oscillating region is rotating into the field-of-view of the CDS slit. This change in the location of the oscillations can be seen if one looks closely at the lefthand panel of Fig. 5, the X-T plot, where the light and dark ridges occur towards the end of the observation time from pixel 30 upwards, whereas below pixel 30 the ridges occur only towards the beginning of the observation time. Similar results are found for the s20680r01 dataset. From pixels 29–31 the oscillations occur at the beginning of the observation time, with two different frequencies present as in Fig. 7. However, for pixels 32–33 the oscillations occur towards the end of the observation period as some new oscillating region appears to be rotated into the field-of-view. This can be confirmed by closely examining the X-T plot in the lefthand panel of Fig. 6 where the light and dark ridges can be faintly seen.

3.2. Time delays of the oscillations

In the previous section, when describing the location of the oscillations we have only discussed the oscillation frequencies measured from the O v line. However, as mentioned in Sect. 2 we obtained observations over a wide range of temperatures, from the temperature minimum emission of the TRACE 1700 passband to the coronal emission of the Fe XVI line. In this section we shall show that over this broad range of temperatures coherent oscillations are continuously present.

In Fig. 8 we plot time series for the six CDS lines and the three TRACE passbands measured from pixel 28 in dataset s20641r01. Each of the time series of the different bandpasses and lines has been filtered by using a bandpass filtering in Fourier space. The solid black lines show the results of this filtering where a bandpass filtering of 4–7 mHz was used; that is, all frequencies below 4 mHz and above 7 mHz have been removed. The original unfiltered time series are shown as the dot-dash lines for comparison. As pointed out in Sect. 3.1 pixel 28 is one of the pixels that contains emission from the sunspot plume. At the right of this plot we label the different line and passband emission together with their formation temperatures (in the case of the CDS lines). These time series have all been scaled relative to the amplitude of the weakest oscillation, TRACE 1700.

The wavelet analysis for the O v oscillations at this pixel position was already shown in Fig. 3. As pointed out previously, in relation to this wavelet analysis, a main oscillation group occurs between times of ∼15–40 min.

In Fig. 8 the region covered by these times has been marked by vertical dashed lines and further divided into two time intervals, A (between 15–28.3 min) and B (between 28.3–40 min). It is obvious from this plot that oscillations are present at all temperatures from the temperature minimum as represented by TRACE 1700 up to the corona as represented by Fe XVI. We note that in Fig. 8 the Fe XVI line shows a quite "noisy" time series. This is due to the presence of intermittent noise at frequencies >10 mHz as well an oscillation component at ∼7.5 mHz which is present in addition to that of the weaker oscillation component investigated by us at ∼5 mHz.

If we concentrate firstly on time interval A, between 15 and 28 min, it may be noticed that while the three TRACE bandpasses show similar oscillations, e.g. there is a good correspondence in the location of the peaks and troughs in each of the TRACE time series, they show little similarity to the oscillations at higher temperatures, e.g. in He I. Similarly the three CDS lines of He I, O III and O V, while similar to one another, do not show a good correspondence with the coronal lines of Mg IX, Mg X and Fe XVI.

The reason for this lack of correspondence between the emission in different temperature regions can be explained by the presence of time delays between the different time series. By using the Fourier time series analysis techniques outlined in Doyle et al. (1999), in particular the method of cross-spectral analysis, we calculated the time delays of each of the lines or passbands relative to the lowest temperature TRACE 1700 emission. The resultant measured time delays are shown in column three of Table 2 together with the frequency, 6.25 mHz, at which the time delays were measured. Positive values refer to time lags relative to the TRACE 1700 emission. We note that the measured value of the oscillation frequency is limited by the frequency resolution of the Fourier analysis, which is directly proportional to the temporal length of the time series examined. Therefore, for time series of limited length the frequency resolution is always poor. For this reason in both Tables 2 and 3 in this paper we shall show both the frequency at which the time delays were measured from the Fourier cross-spectral analysis together with a more accurately measured estimate of the frequency obtained by using a sine curve fitting of the time series. As can be seen from Table 2 the fitting of a sine curve to the oscillations in interval A enabled us to estimate a more accurate value of 5.65 mHz (177 s) for the frequency. All time delays obtained in this work were measured at the 95% confidence level, with squared coherencies typically better than ∼0.8. It was possible to obtain squared coherencies at these levels in each case by concentrating on small intervals in the time series, e.g. interval A and B as described here. The errors shown in Tables 2 and 3 are the 95% confidence intervals.

It is found that in some instances (e.g. Mg IX in time interval A) that the time delays become greater than half a cycle, i.e. 80 s at the Fourier frequency of 6.25 mHz. As a consequence, for Mg IX the time lag as measured from the cross-spectral analysis appears as −25 (±16) s, i.e. the 1700 emission *lags* that of the Mg IX line by 25 s. To obtain a more representative result it is necessary to add a full cycle of 160 s (6.25 mHz) to this result. By doing this we find instead that the Mg IX line lags that of the 1700 passband by 135 s. Both these results are shown in Table 2, with the original value and its error shown in brackets. Similarly it is necessary to add a full cycle of 160 s to the value of 74 (±2) s measured for the Mg X line to obtain the correct lag of 234 s. For the Fe XVI line it is necessary to add two cycles (i.e. 320 s at 6.25 mHz) in order to obtain the correct estimate of 344 s for the time delay. (We note that in both Tables 2 and 3 in this section either one or two cycles are typically added to the time delays for the coronal lines of Mg IX, Mg X and Fe XVI in order to obtain the results shown.)

In Fig. 9a we show the result of overplotting all the time series in time interval A, after shifting each of them "back in time" by their respective time delays relative to the TRACE 1700 passband as given in Table 2. The results are shown after applying a bandpass filter of 4–7 mHz. It will be seen from this plot that there is a very good correspondence between the different emission. This plot also serves to indicate that the measured time delays in this interval are correct.

If we refer to the time delays for interval A in Table 2 it will be noticed that there is a general increase in the time delays with temperature. If a wave were travelling upward we might expect the lowest lying emission (i.e. chromospheric) to be affected first and so on with height (temperature) up to the emission from the very heighest levels in the atmosphere (i.e. the corona). Thus, an increase in time delay with temperature and, therefore, one assumes height, appears to indicate the presence of an upwardly propagating wave mode. We shall return to discuss these results in terms of their phase speeds in Sect. 4.

We point out that from the temperature of He I to O V there is, however, a small decrease in the time delay from 67 to 62 s which would suggest the opposite, i.e. downward wave propagation, over this small temperature range. However, it will be noted that this decrease can be easily accounted for within the errors and thus may not be real.

If we now consider time interval B, the time delay results of which are shown in the fourth column of Table 2, we can see considerable differences in comparison to time interval A. The first notable difference is that there is an increase in the frequency of oscillation, from 6.25 (5.65) mHz in interval A to 7.14 (6.45) mHz in interval B. While we see increases in time delay with temperature up to the TRACE 1550 passband temperature (and perhaps up to the temperature of O III if we discount the more uncertain results from the He I line), we find that the time delays *decrease* from O III up to Mg IX, i.e. at temperatures spanning the whole transition region. A decrease in time delays for these lines relative to the 1700 passband strongly suggests *downward* propagating waves, i.e. in this situation the Mg IX emission leads that of O V by 10 s. The situation changes abruptly at the etemperature of Mg X

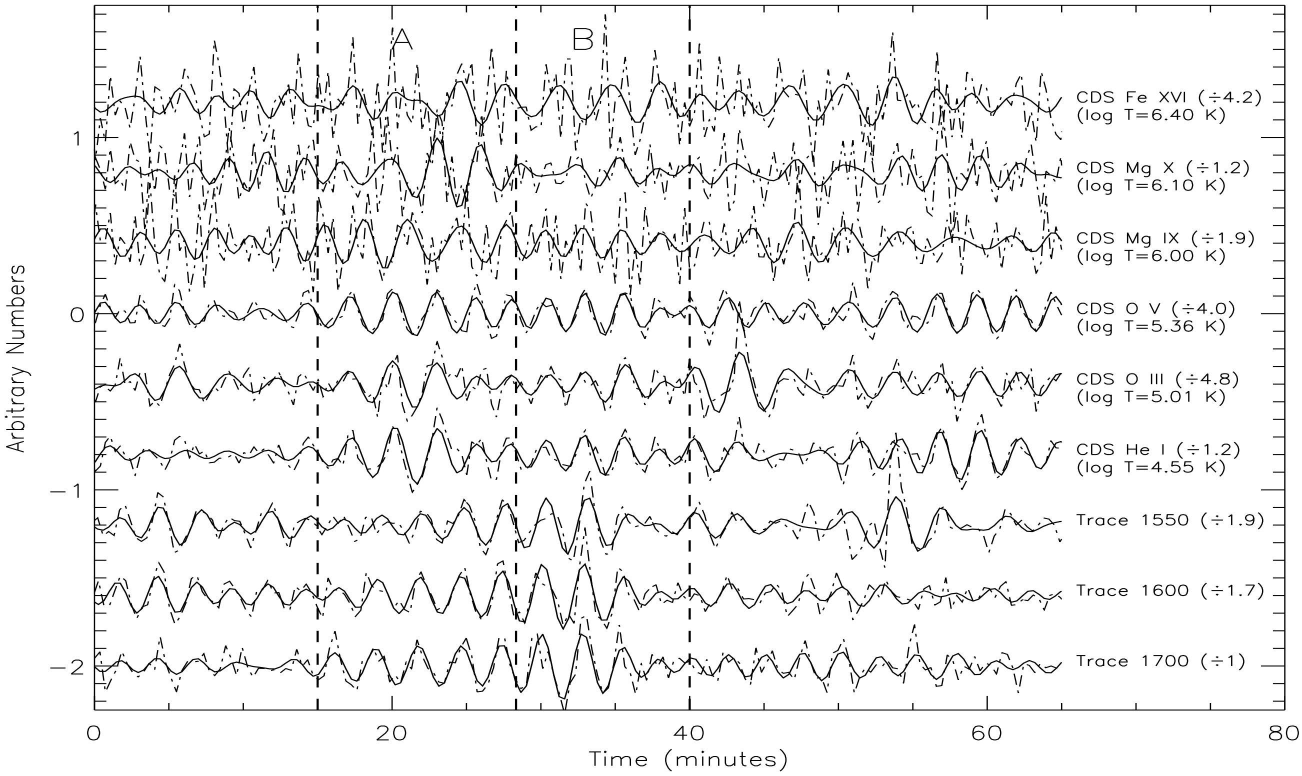

Fig. 8. Time series of all TRACE and CDS data from pixel 28 of s20641r01. Time intervals A and B between 15 and 40 min are marked by the dashed lines. Note that the factors by which each time series has been scaled are shown in the brackets to the right of the line indentifications.

where the time delays increase to 139 s, again suggesting upward propagation, before reaching a value of 309 at the temperature of Fe XVI. These results strongly suggest a change in the nature of the wave propagation at the temperatures between Mg IX and Mg X, i.e. at the start of the coronal region.

In Fig. 9b we overplot all the time series for time interval B after shifting them back by their respective time delays in seconds as given in Table 2. The results are shown in Fig. 9b. As can be seen there is again a good correspondence between the time series of all the different temperature emission.

We find therefore in these results that, within the 25 min spanned by intervals A and B in pixel 28, there is a rapid change in the nature of the wave propagation within a very short period of time. As the Sun rotates >9 arcsec/hr at the coordinates of these observations, we may estimate that, over the 25 min spanned by intervals A and B, a ∼4 arcsec region in the X direction rotated through the 4 arcsec width slit. It is likely therefore that what we are seeing is emission from two different spatial regions, and hence from different umbral structures (each ∼2 arcsec wide), and not the change in frequency of the same spatial region with time.

In Table 2 we also present results for neighbouring pixels 26 and 27, part of the same group of pixels from 24–29 that includes pixel 28 and which also showed high frequency values in Fig. 4. The time delays and measured frequencies for pixel 27 come from oscillations present between ∼5–25 min, the corresponding region to that examined in time interval A of pixel 28, i.e. pixel 28A. The time delays in the oscillations between ∼5–25 min were measured at the frequency of 5.71 mHz in the cross-spectral analysis. The frequency of these oscillations from a more careful sine wave fitting of the oscillations was found to be 5.60 mHz (179 s). We note in passing that the plot of frequency versus position in Fig. 4 showed a value of 6.6 mHz for pixel 27. However, the frequency value of 6.6 mHz shown in Fig. 4 is an *average* over the whole ∼66 min of the observations, while the frequency shown here is from only a portion (∼5–25 min) of this time. The frequency in this pixel thus can vary from between 5–7 mHz at different times over the course of the full observation time.

We can see from Table 2 that pixel 27 shows time delays that are almost identical to those of pixel 28A. Again there is a decrease in time delay between the O III and O V lines as found in pixel 28A. This decrease is however again within the errors. We note that we do not find evidence of two seperate intervals of oscillation here as in pixel 28, with only the oscillations between ∼5–25 min showing a good correspondence at all temperatures up to Fe XVI. By shifting all the lines and passbands back in time by the amounts in seconds shown in Table 2, and overplotting them, we get the result shown in Fig. 10. In the top panel of this plot we show the original unfiltered time series. Even without the filtering it is possible to see common oscillations in all lines between ∼5–25 min. In the

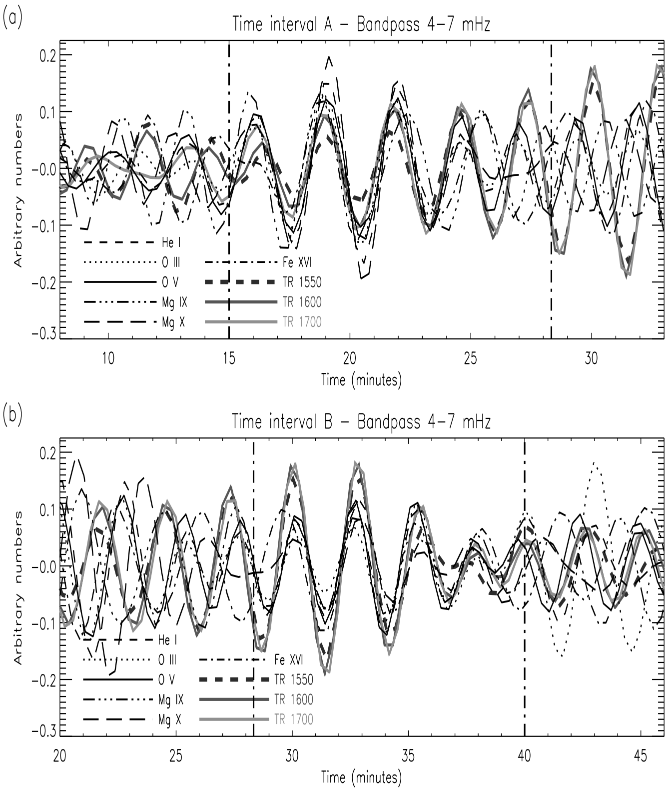

Fig. 9. a) Time series of all TRACE and CDS data from pixel 28 of s20641r01 overplotted after being shifted back in time by their respective time delays relative to TRACE 1700. Time interval A is marked by the dot-dashed lines. **b)** Similarly for time interval B, where again the location of the time interval is marked by the dot-dashed lines.

bottom panel, after applying a bandpass filter of 5–7 mHz, the good correspondence between the oscillations, particularly between ∼10–25 min, can now be seen more clearly.

For pixel 26 the time delays are slightly smaller than those found in pixels 27 and 28A, but again they show the same general pattern, i.e. time delays increasing with emission temperature. In Fig. 11 we show, for pixel 26, the original unfiltered results in the top panel and the filtered results in the bottom panel. As can be seen, the filtering successfully removes the "noise" from the data. An oscillating group between ∼5–18 min is clearly visible in the filtered data. The time delays in pixel 26 were measured at a frequency of 5.33 mHz from the Fourier analysis with its limited frequency resolution. We find that from a more accurate measurement with sine curve fitting that the oscillations in the interval ∼5–18 min have a frequency of 5.60 mHz (179 s). We note that pixel 26 and 27 share the same frequency of oscillation.

The oscillating region examined for pixel 26 is between ∼5–20 min and corresponds to the regions already discussed in pixels 27 and 28A. In fact, the region responsible for the oscillations appears to move in time as we go from pixel 26 to pixel 28, i.e. it shifts from the interval ∼5–18 min in pixel 26, to ∼5–25 min in pixel 27 and to 15–28.3 min in pixel 28A, suggesting an oscillating body that crosses the CDS slit diagonally.

Table 2. Time delays (seconds) relative to the TRACE 1700 passband and the frequencies (from the Fourier analysis) at which they were measured for the Sep. 23 data. The frequencies shown in brackets are those calculated from a sine curve fitting of the oscillations.

Pixel	26	27	28A	28B
Freq.	(5.60)	(5.60)	(5.65)	(6.45)
(mHz)	5.33	5.71	6.25	7.14
1600	2 (1)	7 (4)	4 (2)	6 (2)
1550	6 (3)	21 (12)	17 (8)	19 (5)
He I	36 (21)	66 (2)	67 (5)	15 (12)
O III	34 (20)	68 (12)	66 (5)	21 (5)
O V	23 (12)	61 (7)	62 (7)	16 (4)
Mg IX	125	153	135	6 (2)
	[−63 (7)]	[−22 (10)]	[−25 (16)]	(–)
Mg X	203	227	234	139
	[15 (5)]	[52 (10)]	[74 (2)]	[−1 (2)]
Fe XVI	359	367	344	309
	[−16 (12)]	[17 (19)]	[24 (9)]	[29 (7)]

All three pixels (26, 27, 28A) show evidence of a decrease in the time delays between the O III and O V lines. While these decreases are within the errors in each case it is clear that there is a definite downward trend in all three pixels and this would suggest that these decreases in time delay are real. If this is the case, then, as the O V line leads the O III line in time, this would indicate downwardly propagating waves. This assumes that O V with its higher formation temperature is formed higher in the atmosphere. This would mirror what we see more clearly in time interval B of pixel 28 (i.e. pixel 28B) where the decrease in time delays up to the temperature of Mg IX is much more pronounced. For pixel 26, 27 and 28A and B it is noticed that the He I line shows time delays greater than or at least of the same order as those of the higher temperature O III and O V lines, perhaps suggesting a formation height at or above that of O III.

We note here as an aside that He I is thought to have a complex formation history and thus its emission may not correspond to that which one might expect from a line with its chromospheric formation temperature. In fact, we note that in the raster images the He I line shows features that are otherwise only visible in the coronal lines of Mg IX and Mg X. It is thought that there are two main mechanisms by which He I can form (Andretta & Jones 1997); either by collisional excitation in the lower transition region from electrons with kinetic temperatures higher than the local temperature of the helium atom or by a process in which coronal photons penetrate into the chromosphere and photoionize helium atoms which then recombine to form He I. We note therefore that the emission from He I can reflect conditions at temperatures above that of its putative formation temperature.

We point out that all pixels, 26, 27 and 28A, show large differences of between ∼80–100 s in the time delays between the Mg IX and Mg X lines, which may be considered unusual for lines with such close formation temperatures.All the points touched on here shall be discussed further in Sect. 4.

As mentioned in Sect. 2 no TRACE data was available on the 26 Sep. for a simultaneous comparison with the CDS datasets s20680r00 and s20680r01 of the same day. As a result, for these datasets, we measure the time delays relative to O V as this is the strongest and most reliable CDS line at "low" temperature. We show in Table 3 the results of the time delays measured in the different CDS lines relative to the O V line for two pixels, 27 and 28, from dataset s20680r00 and one pixel, 29, from dataset s20680r01.

We saw previously, in Fig. 7, that pixel 27 of dataset s20680r00 contained two seperate frequencies of oscillation, one at ∼8.5 mHz that is present for the first 20 min and which is then replaced by one at a lower frequency of ∼5.5 mHz that lasts until the oscillations disappear completely at ∼35 min. In the first column of Table 3 we show the time delays for each of these two frequency components, together with their measured frequencies of oscillation.

As the high frequency component occurs first during the time sequence shown in Fig. 7 we shall begin by discussing it, before then seperately discussing the low frequency component.

The high frequency component of the oscillations, that occurs during ∼8–20 min of the observation, has been found (using sine curve fitting) to have a frequency of oscillation of 8.85 mHz (113 s). The time delays for this component shown in Table 3 indicate that the O V oscillations leads all the other lines in time. We note that it is curious that the He I line should lag that of O V as this would indicate that the He I line is formed at a height *above* that of the O V line, assuming upwardly propagating waves. It might have been expected that the He I line would lead that of O V line in time given its lower formation temperature of $\log T = 4.55$ K, and, hence, assumed lower height in the chromosphere. From this result, and assuming we are looking at upwardly propagating waves, it would appear that the He I line is formed at a height above that of O V, and thus somewhere in the transition region. This would fit in with what we have discussed previously, i.e. that the He I line has a complex formation history and can reflect conditions at higher temperatures than its nominal formation temperature. However, another possibility is that the waves are instead propagating downwards from the temperature of O V to the temperature of He I. This would also explain the fact that the He I line lags that of O V. (This shall be discussed more fully in Sect. 4). Supporting evidence for the possibility of downwardly propagating waves also comes from the O III results which with a value of 1 s, indicate that the O III oscillations lag those of O V, which we would not expect for an upwardly propagating wave. In this instance though the small value and large relative error make this result more doubtful. We shall return to discuss these results in Sect. 4. The time delays increase with temperature for the three coronal lines, from 74 s at Mg IX to 180 s at Fe XVI, again possibly suggesting the upward propagation of waves, similar to what we saw previously for the 23 Sep. data.

In Fig. 12a we overplot the time series for all the lines, after shifting them back by their respective time delays relative to O V and applying a bandpass filter of 7–10 mHz to remove the low frequency component. For these high frequency oscillations it will be noticed that all the lines show very similar oscillations between 0–20 min, at which point the oscillations disappear almost completely. The good correspondence between the oscillations at each temperature reinforces the idea that there is some connection between the oscillations at each temperature as well as providing a test of the measured time delay values.

As mentioned above, the time series of pixel 27 also contains low frequency oscillations of ∼5.5 mHz frequency. In Table 3 we show the time delays measured for this component at the frequency of 5.56 in the Fourier analysis. By fitting a sine curve to the data the frequency of the oscillations was measured to be 5.40 mHz (185 s). We can see from the time delays that, as for the high frequency component, the O V oscillations leads all the other lines in time, except for O III, which it lags by 1 s. The fact that O III leads O V suggests that the disturbance causing the oscillations travels up from the lower temperature region of O III. However, the large error in this result, due in large part to the weakness of the O III line, makes the result uncertain. For the other lines we note that He I is again delayed relative to O V, as it was for the high frequency oscillations and also that the time delay of the higher temperature Mg X line is less than that of the lower temperature Mg IX line. That is, the higher temperature Mg X line (which we assume to be formed at a greater height) leads in time the lower temperature Mg IX line, suggesting a downwardly propagating wave at these temperatures. At the temperature of Fe XVI the time delays relative to O V increase again, suggesting a possible renewed upward propagation at this temperature.

In Fig. 12b we show all the lines overplotted, after being filtered with a bandpass of 5–7 mHz in order to isolate the low frequency component. We note the good correspondence between all the lines especially between the times of ∼18–30 min. The low frequency oscillations are present during the first 18 min of the observations and occur simultaneously in time with the higher frequency oscillations shown in Fig. 12a.

Pixel 28, part of the same oscillating group as pixel 27 (see Fig. 5 in the previous section) shares similar oscillation characteristics (i.e. the presence of both high and low frequencies over the observing time.) However, whereas pixel 27 showed two dominant frequencies over the observation time, pixel 28 shows three, at 9.09 (8.85), 7.14 (7.65) and 5.41 (5.40) mHz. We note that both pixels share identical frequencies of oscillation at 5.40 and 8.85 mHz.

Table 3. Time delays (seconds) relative to the O v line and the frequencies (from the Fourier analysis) at which they were measured for the Sep. 26 data. The frequencies shown in brackets are those calculated from a sine curve fitting of the oscillations.

Pixel	27	27	28	28	28	29	29
Freq.	(5.40)	(8.85)	(5.40)	(7.65)	(8.85)	(5.65)	(8.85)
(mHz)	5.56	8.33	5.71	7.14	9.09	5.56	9.23
He I	25 (6)	19 (6)	24 (7)	17 (6)	19 (7)	16 (10)	23 (5)
O III	−1 (10)	1 (1)	−7 (2)	−3 (8)	0 (1)	−2 (1)	1 (1)
Mg IX	149	74	155	151	38 (20)	101	29 (9)
	[−31 (13)]	[−46 (7)]	[−20 (8)]	[11 (4)]	[–]	[−79 (4)]	[–]
Mg X	123	96	162	214	83	219	51 (5)
	[−57 (12)]	[−24 (4)]	[−13 (5)]	[−66 (34)]	[−27 (10)]	[39 (17)]	[–]
Fe XVI	262	180	268	278	202	294	114
	[82 (33)]	[60 (14)]	[−82 (9)]	[−2 (1)]	[−18 (11)]	[−66 (42)]	[6 (10)]

Table 4. Relative amplitudes of oscillation (%) and frequencies at which they were measured for the Sep. 23 data.

Pixel	26	27	28A	28B
Freq.	(5.60)	(5.60)	(5.65)	(6.45)
(mHz)	5.33	5.71	6.25	7.14
1700	1.28	2.55	3.72	4.04
1600	4.09	4.05	4.99	6.77
1550	4.64	6.79	4.16	5.31
He I	4.28	4.77	4.32	3.09
O III	13.06	17.48	14.95	9.89
O V	9.87	14.87	13.51	11.09
Mg IX	4.80	6.87	6.18	5.03
Mg X	0.80	4.73	6.29	1.54
Fe XVI	20.93	17.61	7.63	6.24

In Fig. 13 we overplot all the time series for each of these frequency components, using bandpass filters of 8–10, 7–8 and 5–7 mHz, 7–8 mHz to isolate each of the seperate oscillation components. The delay amounts by which each line has been shifted back relative to O v are given in Table 3, together with the frequencies, from the Fourier analysis, at which the time delays were calculated. If we look at Fig. 13a we can see that the high frequency 8.85 mHz oscillations between 0–19 min occur simultaneously, over part of this time, with oscillations at 7.65 mHz, which occur between ∼10–26 min (see Fig. 13b). In turn we can also see that there is an overlap between the oscillations at 7.65 mHz and those at 5.40 mHz (Fig. 13c), which take place between ∼8–35 min. The 5.40 mHz oscillations only show a good correspondence between all the lines between the times of ∼18–28 min.

We note therefore from the above that different frequencies of oscillation can exist together during the same time intervals, e.g. during the first 20 min of the observations, O v contains oscillations at 5.40 mHz, 7.65 and 8.85 mHz. This suggests that we are seeing overlapping oscillating groups, with different frequencies, in the same location. We point out that this is not an effect of solar rotation as was suggested as an explanation by Fludra (2001) for the number of power peaks at different frequencies generally seen in Fourier power spectra in umbral regions.

We shall now examine the time delays for each of the frequency components in more detail, starting with the 8.85 mHz mode oscillations. Looking at Table 3 we can see that the time delays for this mode (measured at a frequency of 9.09 mHz in the Fourier analysis due to the limited frequency resolution of this analysis) are significantly different than those found for the same 8.85 mHz mode in pixel 27. In particular, the difference between the time delays measured in the Mg IX and Mg X lines is 22 s in pixel 27 but 45 s for pixel 28. In addition, the time delays between the Mg X and Fe XVI lines in pixel 28 is 119 s but in pixel 27 this difference is 84 s. It is possible that the time taken for a wave to travel from one temperature region to another is altered due to a difference in length over which the wave has travelled (i.e. a change in the structure). We note, however, that the non-coronal He I and O III lines show almost indentical values to those in pixel 27, the positive value again possibly suggesting downwardly propagating waves.

For the lower frequency 5.40 mHz oscillations we find broadly similar results to those seen in pixel 27, i.e. He I lags the O v line time, while O III leads it in time. This suggests that the oscillations in this case travel upwards from the O III to the O v line, indicating an upwardly propagating wave, while the time lag of the He I line relative to the O III and O v lines would perhaps in this case indicate downwardly propagating waves from the temperature of O III to the temperature of He I. For this pixel we do not see the decrease in time delay from Mg IX to Mg X as we saw in pixel 27, but instead an increase in the time delays up to Fe XVI. If we assume these lines are formed at sucessive heights in the atmosphere this would again suggest upwardly propagating waves at these temperatures. We note that the difference in the time delays of the Mg IX

Table 5. Relative amplitudes of oscillation (%) and frequencies at which they were measured for the Sep. 26 data.

Pixel	27	27	28	28	28	29	29
Freq.	(5.40)	(8.85)	(5.40)	(7.65)	(8.85)	(5.65)	(8.85)
(mHz)	5.56	8.33	5.71	7.14	9.09	5.56	9.23
He I	1.31	1.67	1.35	1.62	1.57	0.79	0.80
O III	4.86	14.21	9.67	6.80	7.22	9.99	2.90
O V	7.23	11.32	6.03	6.42	7.87	9.21	8.39
Mg IX	9.14	2.88	2.91	2.91	4.41	6.23	11.06
Mg X	1.48	1.95	0.96	0.23	2.19	4.08	3.62
Fe XVI	1.34	5.10	3.77	2.85	2.35	7.67	2.51

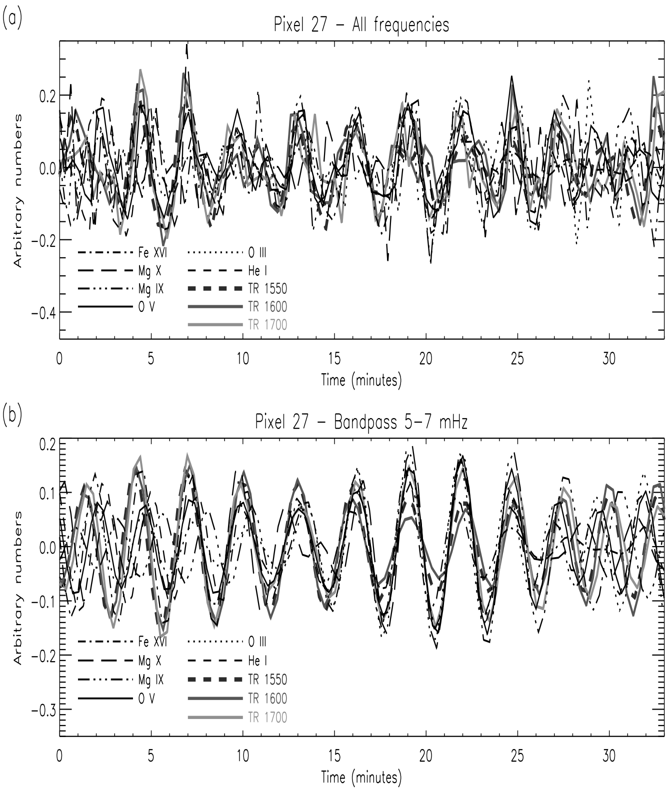

Fig. 10. a) Unfiltered time series of all TRACE and CDS lines for pixel 27 of s20641r01 overplotted after been shifted back in time by their respective time delays relative to TRACE 1700, **b)** the same overplotted time series after being filtered by a bandpass filter of 5–7 mHz.

and Mg X lines is only 7 s here. The 7.65 mHz oscillation mode (measured at 7.14 mHz in the Fourier analysis), shows very similar values to those of the 5.40 mHz mode, except perhaps for the Mg X line which shows large time delays of 214 s relative to the O V line. However, the large errors involved in the measurement of this time delay (i.e. ±34 s) means that there is a large uncertainty associated with this particular result. We can conclude from the closeness in the time delay values between these two lower frequency modes that the waves which cause them probably pass through similar physical conditions or structures.

As a final example of these type of oscillations we plot in Fig. 14 the results for pixel 29 of dataset s20680r01. This dataset was obtained approximately one hour after dataset s20680r00 (see Table 1) and in a slightly different location in the sunspot (see Fig. 2). Yet, we see similar behaviour here, in that we also see the presence of two different oscillation modes, one at ∼9 mHz and the other at ∼5.5 mHz. In Fig. 14a we show the high frequency oscillations for this pixel after all lines had been shifted back by their respective time delays relative to the O V line. These time delays are shown in Table 3 together with the frequency of 9.23 mHz at which they were measured from the Fourier analysis. From a measurement using sine curve fitting we obtained the more accurate value of 8.85 mHz for the oscillations occurring between 2–9 min, a value identical to that found for the high frequency oscillation mode in pixels 27 and 28. The time delays are similar in magnitude to those seen in pixels 27 and 28 of dataset s20680r00 for similar high frequency oscillations. We again see that the He I line lags that of O V and that in the coronal lines the time delays increase with temperature of line formation, indicating a possible upward wave progression. We note from Fig. 14a that there is evidence of high frequency oscillations out to ∼35 min in all the lines but with a poor correspondence between the lines after ∼10 min. The fact that they no longer correspond after this time points to the fact that at these later times the different lines no longer possess the same time delays with respect to the O V line, and each other, as they did for the first 10 min. We have confirmed this by measuring the time delays of certain lines in the range 10–20 min, e.g. we find in this range that O III leads the O V line by 26 s. The reason that these time delays change is most likely related to the fact that over time a different region of the Sun rotates through the slit, with a corresponding change of structure and hence different travel times for waves between the different temperatures.

We find that the low frequency oscillation component occurs simultaneously with the high frequency component between 10–35 min (see Fig. 14b). Note that we show the low frequency oscillations here after filtering with a bandpass of 5–6 mHz to remove the presence of a weak 7 mHz oscillation in some of the lines. From Table 3 we can see that the accurately determined frequency (from sine

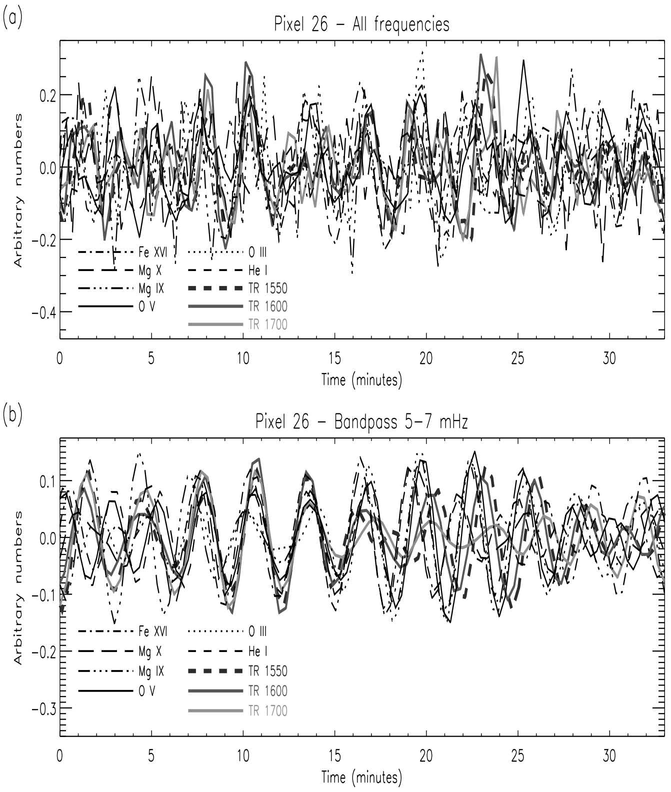

Fig. 11. a) Unfiltered time series of all TRACE and CDS lines for pixel 26 of s20641r01 overplotted after been shifted back in time by their respective time delays relative to TRACE 1700, **b)** the same overplotted time series after being filtered by a bandpass filter of 5–7 mHz.

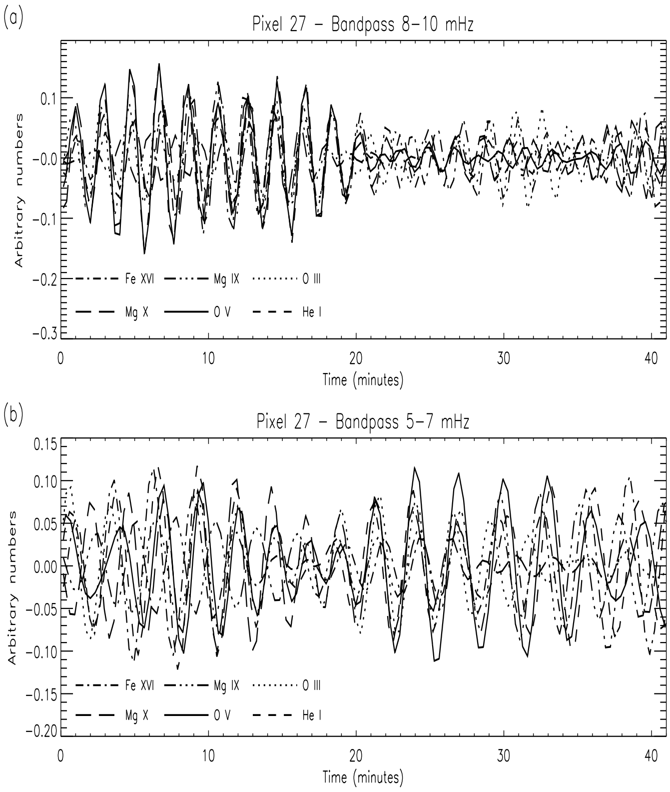

Fig. 12. a) 8–10 mHz bandpass filtered time series of all TRACE and CDS lines for pixel 27 of s20680r00 overplotted after been shifted back in time by their respective time delays relative to CDS O V, **b)** 5–7 mHz bandpass filtered time series for the same pixel after been shifted back in time by their respective time delays relative to CDS O V.

curve fitting) for these oscillations is a value of 5.65 mHz. The time delays show similar characteristics to those seen previously, with increasing time delays with temperature in the coronal lines and He I showing a lag relative to the O V line. We note however that the large difference in time delay between the Mg IX and Mg X lines indicates a marked difference in wave propagation in this region. For example in pixel 28 the time delay between these two lines was only 7 s but here it is 118 s. We shall return to this point in the Sect. 4. It will be noticed from Fig. 14b that during the first ∼10 min of the observations, the location of the 8.85 mHz oscillations, that the low frequency oscillations are very weak. For the rest of the observation time the 5.65 mHz oscillations are strong, with the best correspondence between the lines for this component occurring between 15–23 min. However, as can be seen in Fig. 14a this is also the time during which high frequency oscillations are present. So again we have a situation where two frequencies are present simultaneously and co-spatially in a time series.

3.3. Amplitudes of the oscillations

In this section we present results of the measurement of the relative amplitudes of oscillation in the different lines. The amplitude estimates were obtained from the Fourier power spectra, where the peaks in the power spectra at the different frequencies are proportional to the square of the oscillation amplitudes at these frequencies. Before carrying out this analysis it was necessary to remove the contribution of the low frequency background emission on which the umbral oscillations are superimposed (i.e. to obtain the relative intensity). In order to do this we follow the method already outlined in Sect. 3.1, i.e. we calculate the background trend by using a 30 point running average which we then divide into the data and subtract a value of 1.

In Table 4 we show the measured amplitude values for the TRACE passbands as well as the CDS lines. The amplitudes were measured at the same frequencies used to estimate the time delays in Tables 2–3. In Table 4 we also show in brackets the frequencies measured from sine curve fitting, which give a more accurate estimate for the frequencies in each case. From Table 4 we can see that for pixels 26 and 27 the amplitudes increase from the temperature minimum region as represented by TRACE 1700 up to the lower chromosphere as represented by TRACE 1550, before showing a minimum at the temperature of He I in the upper chromosphere/transition region. For pixel 28A the increase in amplitudes is only present between TRACE 1700 and TRACE 1600, which

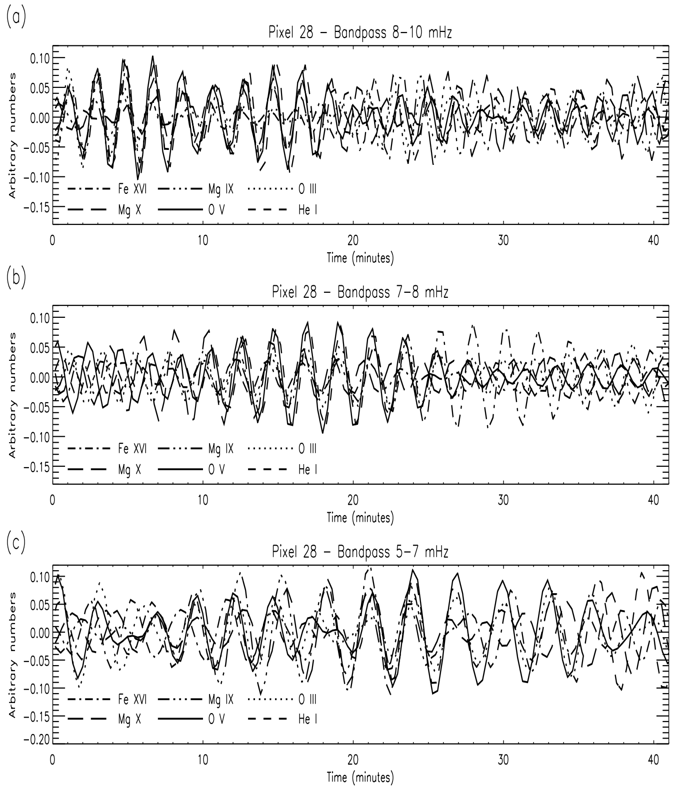

Fig. 13. a) 8–10 mHz bandpass filtered time series of all TRACE and CDS lines for pixel 28 of s20680r00 overplotted after been shifted back in time by their respective time delays relative to CDS O V, **b)** 7–8 mHz bandpass filtered time series for the same pixel, **c)** 5–7 mHz bandpass filtered time series for the same pixel.

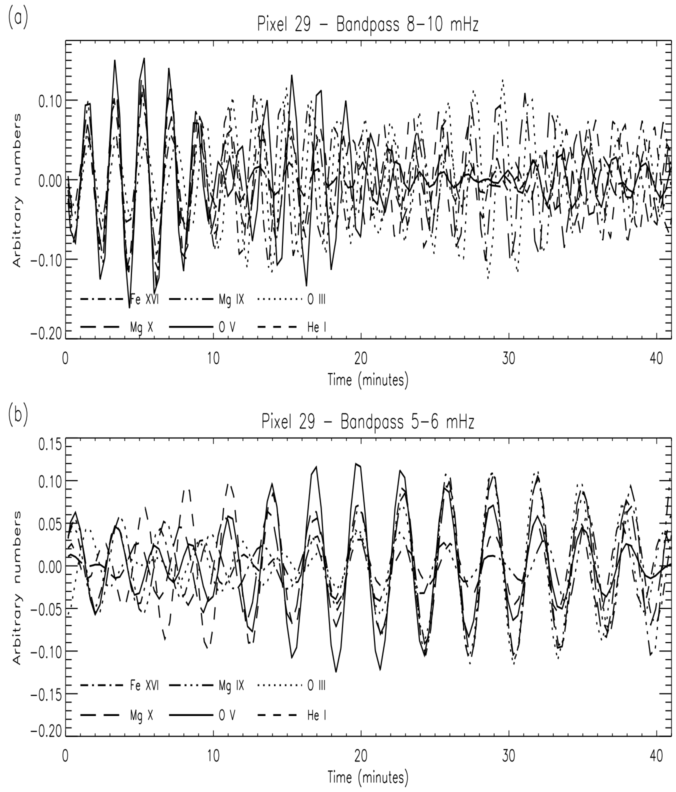

Fig. 14. a) 8–10 mHz bandpass filtered time series of all TRACE and CDS lines for pixel 29 of s20680r01 overplotted after been shifted back in time by their respective time delays relative to CDS O V, **b)** 5–6 mHz bandpass filtered time series for the same pixel after been shifted back in time by their respective time delays relative to CDS O V.

contains emission from just above the temperature minimum region, before there is a decrease at the temperature of TRACE 1550. For pixel 28B the increase is also only present between TRACE 1600 and 1700 before the amplitudes decrease to a minimum at the temperature of He I. In Fig. 15a we plot the amplitudes for the CDS lines (from Table 4) as a function of their formation temperatures. We have not plotted the amplitudes of the TRACE passbands in this plot due to their uncertain formation temperatures. It can be seen that for all the pixels the trend from the temperature of He I up to Fe XVI is broadly similar, that is, there is an increase in the amplitude by a factor of ~3–4 at the temperature of O III, where pixels 26, 27 and 28A show their maximum amplitude; pixel 28B shows its maximum amplitude at the temperature of O V, before the amplitudes decrease to a minimum at the temperature of Mg X or Mg IX in the case of pixel 28A. At the temperature of Fe XVI all the pixels again show increases in their amplitudes. In pixels 26 this increase is particularly large with the relative amplitude increasing to a value of ~21%, with an increase by a factor of ~25 in relation to its minimum value at Mg X.

In Table 5 we show the relative amplitudes for the 26 Sep. CDS data together with the frequencies at which they were measured. The amplitudes were measured for each of the low and high frequency components found in the three pixels 27, 28 and 29 and which were discussed in the previous section. We plot these results graphically in Figs. 15a, b and c as an aid to their interpretation. As can be seen in Fig. 15b, for pixel 27, the low and high frequency components do not exhibit identical variations with temperature. The high frequency oscillation amplitudes shown with the dark line in this plot follow the variations that we saw in Fig. 15a for the 23 Sep. data, i.e. a peak at O III, a minimum at Mg X and an increase at Fe XVI. The low frequency oscillations follow a different pattern with the steady increase in amplitude up to the temperature of Mg IX before a rapid decrease at the temperature of Mg IX and then a subsequent smaller decrease at the temperature of Fe XVI. Both components, however, do show similarities, with both having practically identical amplitudes at the temperature of He I and with both showing a decrease in the value of the amplitude at the temperature of Mg X. For pixel 28, the amplitudes of the three frequency components, measured at 5.71 (5.40), 7.14 (7.65) and 9.09 (8.85) mHz, show variations like those seen in the Sep. 23 data. The two components at 5.71 (5.40) and 7.14 (7.65) mHz show very similar variations in the amplitudes, mirroring the similarities found between the time delays in these two components (see previous section). The high frequency component at 9.09 (8.85) mHz has a slightly different variation with the maximum amplitude occurring at the temperature of O V and not O III as for the other two components. In this it mirrors the variation seen for the 7.14 (6.45) mHz component in the pixel 28B data shown in Fig. 15a. We note that again all the frequency components in this pixel show sharp declines in their amplitudes at the temperature of Mg X. If we now examine Fig. 15c for results of pixel 29 we can see that it shares the same pattern as seen for pixel 27, except that this time it is the high frequency component that shows its maximum at the temperature of Mg IX, while the low frequency component follows the, by now, more standard variation, i.e. a peak in the amplitudes at O III and a minimum at Mg X.

So from the above discussion we can see that the amplitude data shows a number of common features, irrespective of the pixel or region examined on either day. For the 23 Sep. data there is evidence for three different temperature zones, one in the chromosphere between TRACE 1700 and He I, with the minimum in the measured amplitudes generally at He I, one in the transition region between the temperatures of He I and that of Mg X, where another minimum is reached, and one in the upper corona at temperatures above that of Mg X, i.e. at the temperature of Fe XVI measured here. The maximum in the amplitudes generally occurs at the temperature of O III. For the 26 Sep. data we have no information on the chromosphere, except perhaps for the He I line, but we find that the transition region and coronal lines broadly follow the same pattern as for the 23 Sep. data. The only large variations we have seen were in the low frequency component of pixel 27 and the high frequency component of pixel 29 for the 26 Sep. data, where the maximum in the relative amplitudes occurs at the temperature of Mg IX and not the more typical temperature of O III or O V. We note that these two components also do not show the usual increase in the amplitude at the temperature of Fe XVI but rather a slight decrease. From an examination of all plots in Fig. 15 it is clear, however, that the main pivotal point is at the temperature of Mg X where all lines usually show a sharp decline in their measured amplitudes. This sharp decline occurs between the temperatures of Mg IX and Mg X on the border of the corona.

4. Discussion

For the 23 Sep. data shown in Table 2 we find that up to the temperature of O III the time delays increase, suggesting upwardly propagating waves. We note that the He I line sometimes shows an exception to this but as pointed out earlier He I has a complicated formation history and its emission may reflect conditions at higher temperatures or heights in the atmosphere. The time delays for the O III line measured relative to TRACE 1700 are 34, 68, 66 and 21 s for pixels 26, 27, 28A and 28B respectively. We note that we can estimate the approximate height of O III in the umbral atmosphere by using the results of the sunspot model of Obridko & Staude (1988). Reading off from Table 2a in their paper the temperature of O III corresponds to a height of ∼2200 km in the atmosphere (after adding in the value for the Wilson depression). If we assume that TRACE 1700 is formed at an approximate height of ∼400 km (Judge et al. 2001) then the vertical height between the TRACE 1700 region and that of O III is of the order of 1800 km. Using this estimate of vertical height it is possible using the time delays between TRACE 1700 and O III to estimate propagation speeds between these two different temperature regions. By doing this we obtain the speeds of 53 km s^{-1}, 26 km s^{-1}, 27 km s^{-1} and 86 km s^{-1} for pixels 26, 27, 28A and 28B respectively at the temperature of O III. Since the sound speed at the temperature of O III is of the order of 49 km s^{-1} then the propagation speeds in pixel 26 and 28B are supersonic. The Alfvén speed at the same temperature has a value of 460 km s^{-1}, assuming a magnetic field of 3000 G and an average active region density of log 10.52 cm^{-3} (a value obtained by Pérez et al. 1999 using a O IV density diagnostic).

The speeds obtained here for all pixels are clearly closer in magnitude to the estimated value of the sound speed than to that of the Alfvén speed. This would indicate that the oscillations we see are due to slow magnetoacoustic waves. We note that the model of fast magnetoacoustic waves in the photosphere (e.g. Thomas & Scheuer 1982) predicts that one should see acoustic-like waves propagating upwards at the slow wave speed (∼the sound speed) along the vertical magnetic field lines (Thomas 1984). We also point out that Banerjee et al. (2002) have presented new analytical solutions for magneto-acoustic-gravity (MAG) waves including radiative losses in a magnetized atmosphere. They observe different sunspots from CDS and they interpret their observed 3 min oscillations in terms of slow magnetoacoustic modes.

Brynildsen et al. (2001) observed that the downflow in sunspot plumes is maintained by plasma at transition region temperatures streaming in flow channels from locations well outside the sunspot. The downflow is approximately 25 km s^{-1} at temperatures close to that of O V, i.e. 250 000 K. We have seen in this work that there is evidence of upwardly propagating waves in sunspot plume locations (e.g. the discussion of the results of Table 2 in Sect. 3.2). We suggest the possibility that waves (inferred by us from the oscillations) could be propagating up through the downflowing plasma in the sunspot umbra. We point out that one effect of such downflowing plasma in the sunspot would be to shift the observed ions (i.e. O III etc.) from their expected ionization equilibrium temperatures. For example, Doyle et al. (1985) found that temperature diagnostic line ratios of several lines in a sunspot plume yielded temperatures below those expected in ionization equilibrium. They suggested this was caused by cooling falling gas in the sunspot, i.e. downflows can move ions to lower temperature regions quicker than they can cool and recombine to become lower temperature ions.

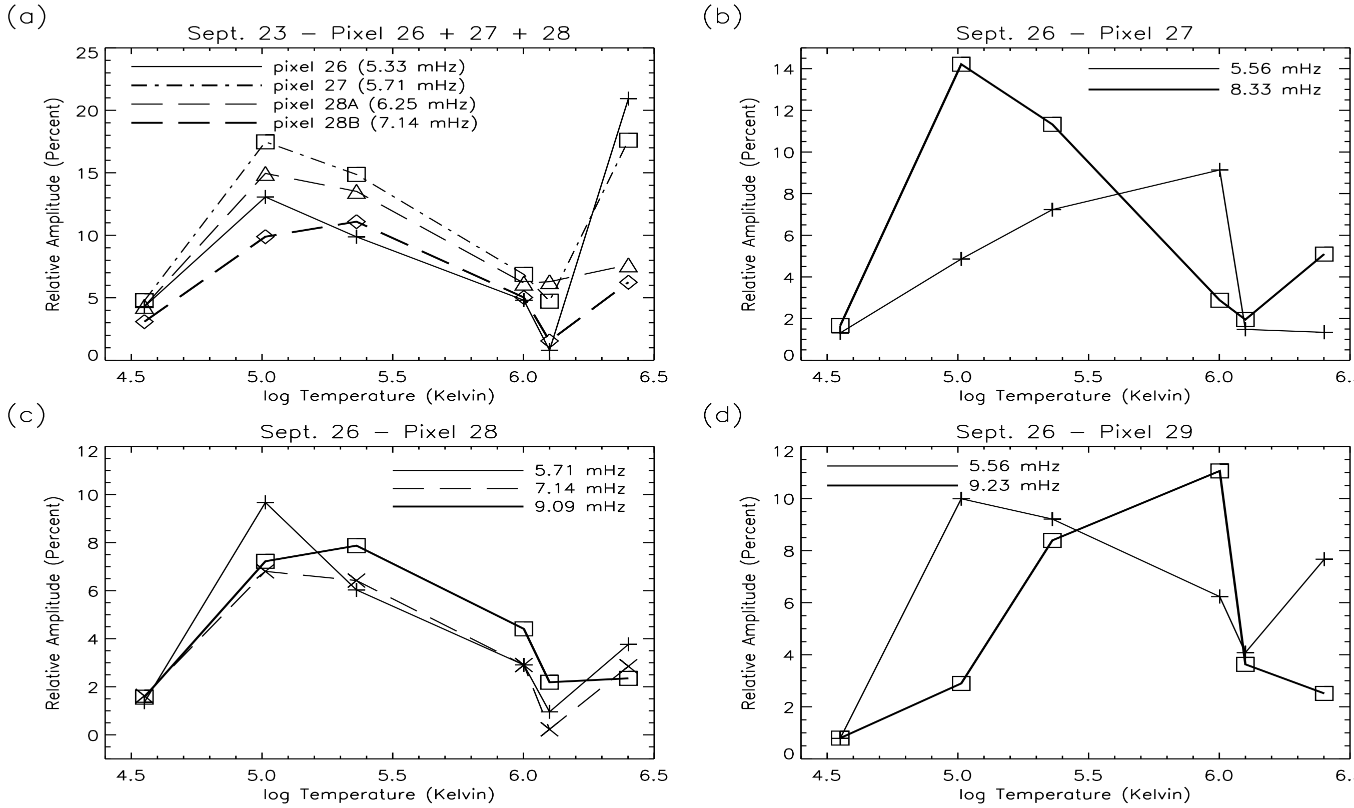

Fig. 15. a) Relative amplitudes versus the line formation temperatures of He I ($\log T = 4.55$ K), O III ($\log T = 5.01$ K), O V ($\log T = 5.36$ K), Mg IX ($\log T = 6.00$ K), Mg X ($\log T = 6.10$ K) and Fe XVI ($\log T = 6.4$ K) for pixels 26, 27 and 28 of Sep. 23. The amplitudes were measured at the same frequencies used to estimate the time delays in the Fourier analysis (Table 2). The pluses represent the results for pixel 26, the boxes the results for pixel 27, the triangles the results for pixel 28A and the diamonds the results for pixel 28B. **b)** The relative amplitudes versus line formation temperature for pixel 27 of dataset s20680r00 for the 5.56 mHz (crosses) and 8.33 mHz (boxes) components. **c)** The relative amplitude versus line formation temperature for the three frequency components at 5.71 mHz (pluses), 7.14 mHz (crosses) and 9.09 mHz (boxes) for pixel 28 of dataset s20680r00. **d)** The relative amplitude versus line formation temperature for the two frequency components at 5.56 mHz (pluses) and 9.23 mHz (boxes) for pixel 29 of dataset s20680r01.

We note that pixels 26, 27 and 28A in the Sep. 23 data showed evidence for a decrease in time delays between the O III and O V lines, which we suggested in the last Sect. 3.2 may be due to downwardly propagating waves. For example, these waves could be reflected waves from the transition region/corona interface. We point out that Brynildsen et al. (2000) suggested that a difference of 205° between maxima in intensity and blue shift in a N V line ($\log T = 5.2$ K) was due to partial wave reflection. However, in Fig. 9 we can see that there is a good correspondence between oscillations at all temperatures of emission, perhaps indicating one wave mode between low and high temperatures. The question is how to reconcile this fact with the apparent presence of both upwardly and downwardly propagating waves. It may be, however, that neither O III nor O V are present at their ionization equilibrium temperatures due to the downflows in the sunspot and are therefore at positions (heights) in the atmosphere not consistent with their formation temperatures. In such a scenario it is perhaps possible that the emission from O V comes from a location *below* that of O III. This would then mean that the slight decrease in the time delays between O III and O V could also be interpreted in terms of upwardly propagating waves. Another possibility is that there are only a small number of preferred frequencies of oscillation allowed in the sunspot and therefore all disturbances whether upwardly or downwardly propagating are constrained to oscillate at one of these set frequencies.

Pixel 28B showed the best evidence of downward propagating waves from O III up to the temperature of Mg IX, i.e. the time delays decrease up to this temperature. The difference in the time delays between O V and Mg IX is 10 s for pixel 28B. If we refer back to Table2a of Obridko & Staude (1988) the vertical height difference between the temperatures of the O V and Mg IX lines is ~560 km and therefore the propagation speed between these two lines is ~56 km s^{-1} i.e. subsonic at the temperature of Mg IX (c_s = ~152 km s^{-1}). We note that Hansteen (1997) discusses the possibility that magnetohydrodynamic waves, created in the corona by reconnection events, which become non-linear as they propagate towards the chromosphere can cause the net redshift seen in transition region lines. In relation to the apparently downwardly propagating waves seen by us in pixel 28B, we suggest the possibility that these are connected to the disturbances proposed by Hansteen (1997). We note in support of this that a number of flaring events are seen close to the location of pixel 28, i.e. at pixels 30–33 which we previously discussed in relation to Fig. 4 in Sect. 3.1. The flaring events between the times of ∼20–30 and ∼40–50 min coincide with broadened Gaussians. Some of these Gaussians at ∼43 min show evidence of the same asymmetry seen by Brynildsen et al. (2001) in their Fig. 24, which they suggested could be caused by the downward propagating magnetohydrodynamic waves proposed by Hansteen. We point out that these flaring events are seen in all the CDS lines up to the temperature of Mg X but are not present in the Fe XVI line, suggesting, perhaps, a change in the structure of the sunspot at this temperature. We can see in Fig. 9b that there is a good correspondence between the oscillations from all temperatures of emission, i.e. between the upwardly propagating oscillations up to O III, the downwardly propagating oscillations from O III up to Mg IX and the upwardly propagating oscillations at Mg X and Fe XVI. This good correspondence between the oscillations again suggests that there may be preferred frequencies of oscillation in the sunspot, and that all disturbances in the sunspot atmosphere are somehow constrained to oscillate at these frequencies.

For the other pixels 26, 27 and 28A the time differences between the time delays of the O V and Mg IX lines are much larger. These are 102, 92 and 73 s for pixels 26, 27 and 28A respectively which would correspond to propagation speeds of only 5.5, 6 and 7.5 km s^{-1}, far smaller than that seen for pixel 28B. For pixels 26, 27 and 28A it is clear that there is some abrupt change in the propagation between the temperature of O III, where we saw propagation speeds of 53, 26, 27 km and the temperature of Mg IX where the propagation speeds are reduced to 5.5, 6, 7.5 km s^{-1}. These low speeds, however, may just reflect the angle at which we view the sunspot, i.e. if we view at a steep angle projection effects may give the impression of lower speeds. It may also be the case that the height between the temperatures of O V and Mg IX is smaller in a dynamic downflowing sunspot environment than that given in Obridko & Staude (1988). We can see from the plots of relative amplitude in Fig. 15 that the amplitudes for pixels 26, 27 and 28A decrease by a factor of 3–4 between the temperatures of O III and Mg IX, mirroring somewhat the decrease in propagation speeds seen between O V and Mg IX. We note that the three pixels show similar variations of their relative amplitude with temperature, i.e. a maximum at the temperature of O III and a minimum at the temperatures of Mg IX and Mg X. Pixel 28B on the other hand, with its slightly higher oscillation frequency of 6.45 mHz, showed some differences in its relative amplitude values, with the maximum occurring at O V while also showing a decrease by a factor of two from this value at the temperatures of Mg X.

It is curious that the shape of the measured line-of-sight velocities shown in Fig. 12 of Brynildsen et al. (2001) or Fig. 18 of Brynildsen (1999c), in their measurement of sunspot plumes, show a not dissimilar variation with temperature as the relative amplitudes plotted by us in Fig. 15a. That is, it appears that the maximum red-shift may occur close in temperature to that of the maximum relative amplitude and follow a similar variation with temperature which may indicate that the red-shifts are related in some way with the umbral oscillations. As we mentioned earlier, it may be that the waves we infer from the oscillations, propagate up through the downflowing plasma in the sunspot. As most of this downflowing plasma is at the temperatures of O III and O V it may then be expected that the largest amplitudes of oscillation would occur precisely in plasma at these temperatures, as we have, in fact, seen in Fig. 15.

Looking at Table 2 it will be noted that for all pixels there are large differences in the measured time delays between the Mg IX and Mg X lines, i.e. from a value of 125 s to 203 s for pixel 26, a difference of 78 s. This large difference might be regarded as peculiar for two lines formed so relatively close in temperature, i.e. Mg IX at $\log T = 6.00$ K and Mg X at $\log T = 6.10$ K. From Table 2a of Obridko & Staude (1988) the height between the temperatures of these two lines is ∼520 km, so that, for the time difference of 78 s measured for pixel 26 the speed of propagation is only 6.7 km s^{-1}. This is very close to the speed measured between O V and Mg IX for the same pixel. Similar results are found for pixels 27 and 28A. Again, we suggest that these low speeds could be due to projection effects or to a smaller distance between the Mg IX and Mg X lines than that given by Obridko & Staude (1988). We note that pixel 28B also shows an abrupt change at the temperature of Mg IX with the time delays increasing from a value of 6 s at this temperature to 139 s at the temperature of Mg X, suggesting a propagation speed of only 4 km s^{-1} at these temperatures. We remind the reader, however, that pixel 28B showed evidence for downwardly propagating waves up to the temperature of Mg IX and so the large time difference between these lines is probably just a consequence of this.

The differences in the time delays between the Mg X and Fe XVI lines for pixels 26, 27, 28A and 28B show large values of 156, 140, 110 and 170 s respectively. From the height difference of ∼15 700 km between these temperatures, estimated from Obridko & Staude (1988), the speeds at the temperature of Fe XVI are 101, 112, 143 and 92 km s^{-1} respectively for pixels 26, 27, 28A and 28B.

We can summarise these results for the Sep. 23 data by pointing out that for all pixels the propagation speeds decrease from relatively large values measured between TRACE 1700 and O III, to much smaller values measured between O V and Mg IX and between Mg IX and Mg X. That is, at temperatures above that of the O V line, i.e. at Mg IX and Mg X the beginning of the corona, there may be an abrupt change and slowing in the propagation speed which is mirrored in a reduction in the relative amplitude of the oscillations. At the temperature of Fe XVI the propagation speed appears to increase again, and this is mirrored in an increase in the relative amplitude of the oscillations.

For the 26 Sep. data (shown in Table 3) large differences in time delay are found between the O V and Mg IX lines for each of the lower frequency oscillation components, i.e. 149 s for the 5.40 mHz component in pixel 27, 155 s (151 s) for the 5.40 (7.65) mHz component in pixel 28 and 101 s for the 5.65 mHz component in pixel 29. These time delays all correspond to very small propagation speeds of $\sim$4–5 km s^{-1} at the temperature of Mg IX. For the higher frequency component (8.85 mHz) of the oscillations the differences are smaller, i.e. 74 s for the 8.85 mHz component in pixel 27 and 29 s for the same component in pixel 29, indicating higher propagation speeds and a less abrupt decrease in the possible upward propagation of the waves. In fact, the value of 29 s for pixel 29 would correspond to a speed of 19 km s^{-1} assuming the vertical height of 560 km between O V and Mg IX. These results suggest some difference in the propagation characteristics of the low and high frequency components. We note that, in general, the high frequency components of pixels 27, 28 and 29 show lower values of time delays than the low frequency components. This perhaps reflects the fact that the waves causing the high frequency oscillations propagate through different structures or conditions than the lower frequency oscillations. For pixel 27 and 29 this difference in the time delays between the low and high frequency components is also reflected in the plots of relative amplitude with both components showing a different variation in the relative amplitude with temperature (see Figs. 15b and d). This was discussed previously in Sect. 3.3. For pixel 28 the relative amplitudes of the 8.85 mHz component are only slightly different than those of the other low frequency components, with the maximum now present at the higher temperature of O V.

For the 26 Sep. data some of the pixels show differences in the time delays between the Mg IX and Mg X lines that are not as large as those seen in the 23 Sep. data. For example, for the low frequency 5.40 mHz component of pixel 27 the difference between the time delays measured in the Mg IX and Mg X lines is only 26 s. As we noted earlier in Sect. 3.2 the fact that the time delays decrease from Mg IX and Mg X in pixel 27 could be indicative of downward propagating waves. We do not see evidence of this decrease in any of the other pixels. Assuming a height difference of 520 km between these lines the time difference of 26 s represents a wave propagating downward at $\sim$20 km s^{-1}. However, as discussed earlier in this section, this apparent downward propagation can also perhaps be explained due to departures from non-ionization equilibrium in downflowing plasma. Other low frequency components such as the 7.65 mHz component of pixel 28 and the 5.65 mHz component of pixel 29 do show larger time delay differences of 63 and 118 s respectively, which would correspond to lower speeds of approximately 8 and 4 km s^{-1}. The small value of 7 s for the 5.41 mHz component of pixel 28, however, would represent a much higher speed of 74 km s^{-1}. The high frequency 8.85 mHz component of pixel 28 shows a delay of 45 s, between Mg IX and Mg X, which corresponds to a propagation speed of 12 km s^{-1} while pixels 27 and 29, for the same frequency component, both show delays of 22 s which correspond to speeds of 24 km s^{-1}.

We note that, as for the Sep. 23 data, all the components show large differences in the time delays measured between the Mg X and Fe XVI lines, e.g. 139 s for the low frequency 5.40 mHz component of pixel 27 or 63 s for the 8.85 mHz component of pixel 29. For all the pixels these time differences correspond to speeds of between $\sim$110–250 km s^{-1} for a height difference of $\sim$15 700 km between these temperatures. This leap in the speed at the temperature of Fe XVI mirrors the increase generally seen in the values of the relative amplitude at the same temperature, from the low value it has at the temperature of Mg X (see Fig. 15).

We shall now summarize the main results for the 26 Sep. below. For the 26 Sep. data we see differences present between the lower and higher frequency components. For the lower frequency components (i.e. 5.40–7.65 mHz) between O V and Mg IX we see results similar to those seen in the 23 Sep. data, i.e. low values of propagation speeds (4–5 km s^{-1}) for all pixels. Again these low speeds may be due to projection effects or to variations in the height between the temperature regions of Mg IX and Mg X (i.e. away from those values given by Obridko & Staude 1988). However, unlike the 23 Sep. data we see that these propagation speeds can in some cases increase between the temperatures of Mg IX and Mg X, i.e. to speeds of 74 km s^{-1} in the case of the 5.40 mHz component of pixel 28. For other pixels, i.e. pixel 29 the propagation speeds remain low at a value of 4 km s^{-1}. For the higher frequency components (i.e. at 8.85 mHz) the propagation speeds are slightly larger than the values seen in the lower frequencies, both between the O V and Mg IX lines and also between Mg IX and Mg X, where they increase slightly. Both low and high frequency components in the Sep. 26 data show a dramatic increase in the propagation speed between Mg X and Fe XVI to values of $\sim$110–250 km s^{-1}.

As for the 23 Sep. data, therefore, we see a change from the lower speeds seen between the temperatures of O V and Mg IX to typically much higher propagation speeds at the temperatures of Mg X and Fe XVI. In the plots of relative amplitude in Figs. 15b, c and d we see that all pixels and frequency components show a minimum at the temperature of Mg X, decreasing from a maximum at either the temperature of O III, O V or Mg IX.

We saw in Sect. 3.2 for the 26 Sep. data that the He I line, and sometimes the O III line, showed unusual time delays that indicated that they lag O V in time. We suggested that these lags could perhaps be explained by waves propagating downwards from the temperature of O III/O V. However, as we have previously mentioned He I may not be a reliable line to use in these circumstances due to its uncertain formation history, i.e. its height in the atmosphere may not conform to its formation temperature. The emission we measure from this line may thus be coming from heights above that of O V, which would fit into an alternative scenario that we are actually seeing upwardly propagating waves. We suggest that the O III may appear to lag O V due to departures from ionization equilibrium which may occur due to downflows flows in the sunspot. A similar argument was used earlier in regard to the apparent time lag between the O III and O V lines in the 23 Sep. data.

From the relative amplitude measurements of the 23 Sep. data we found that the amplitudes tend to reach a minimum at the temperature of He I or TRACE 1550, decreasing from slightly larger values at the temperature of TRACE 1600. We note that Thomas et al. (1987) found a 7.5 mHz oscillation that was present from the photosphere to the transition region but which had a low amplitude in the chromosphere. They suggested that these low amplitudes in the chromosphere could be due to the presence of a node consistent with theoretical models of umbral oscillations as resonant modes of the sunspot atmosphere. Their results would appear to mirror what we seen here, with our amplitudes decreasing to reach a minimum at the chromospheric temperatures of He I and TRACE 1550. This reduction in amplitude of the low temperature emission at chromospheric temperatures mirrors the minimum in amplitude typically seen at the temperature of Mg X in the higher temperature lines (see Fig. 15). It therefore remains a possibility that the reduction in amplitude we see at this temperature is also due to a node of resonant oscillations occurring in the corona. In this scenario, we suggest that the increase in the amplitude seen at the temperature of Fe XVI may be due to some waves tunnelling through the node into the lower density conditions in the corona. This may be also reflected in the fact that, as we have seen, the propagation speeds typically increase between the temperatures of Mg X and Fe XVI lines from very low values between Mg IX and Mg X. However, we note that our inferrance of propagating waves in this work would appear to argue against the presence of resonant modes.

We point out that it was not possible to determine whether the oscillations we see in this work are due to linear or non-linear waves due to the poor velocity resolution of the CDS data. We find that the amplitudes of all the oscillations reach a maximum typically at the temperature of O III (and occasionally at higher temperatures of O V and Mg IX) before decreasing at the temperature of Mg X and then again increasing at the temperature of Fe XVI. This behaviour might not suggest a simple picture of a linear (or non-linear) acoustic wave propagating upwards, where we might expect the amplitude to more or less increase with temperature, as the density decreases. It is possible that the decrease in the amplitudes we see is related to some form of energy dissipation, which is what we might expect from waves steepening into shocks at the start of the transition region (i.e. at the temperature of O III), which is where we, in fact, typically see the largest amplitudes of oscillation (e.g. see Fig. 15). The fact that some of the pixels show the maximum of their amplitudes at temperatures of O V and Mg IX may be indicative of (non-linear) waves that can propagate higher into the atmosphere before dissipating.

It may be, however, that the waves we infer from the oscillations propagate up through the downflowing plasma in the sunspot. As most of this downflowing plasma is at the temperatures of O III and O V it may then be expected that the largest amplitudes of oscillation would occur precisely in plasma at these temperatures, as typically seen in Fig. 15.

A perhaps simpler explanation for the decrease in the amplitudes up to the temperature of Mg X may be that the size of the region in which the oscillations occur is increasing in size with temperature. Therefore, at the temperature of Mg X the line forming region is very broad, perhaps of the order of (or even larger) than the wavelengths of these waves. If a complete wave was contained within the line forming region then we might therefore not expect to see any intensity variations (or Doppler variations). However, we point out that this perhaps would not explain the fact that the Fe XVI line typically shows a large increase in amplitude compared to the minimum amplitude value seen at Mg X.

While we have found a clear relationship between the umbral oscillations and a sunspot plume in Fig. 1 for the 23 Sep. data, we also found that oscillations can be present in the sunspot umbra independently of a plume being present (e.g. Fig. 2 for the 26 Sep. data). This suggests that the oscillations are a property of the sunspot umbral region and can exist independently of sunspot plumes. These results are consistent with the recent results of Maltby et al. (2001), i.e. that plumes located above the umbra show oscillations while plumes located above the penumbra do not which they suggested was because the oscillations they see are a property solely of the umbral transition region.

5. Conclusions

In this paper we have examined oscillations observed in a large sunspot associated with AR 9169 on the 23 and 26 Sep. 2000. We have closely examined oscillations from different umbral regions in the sunspot over a broad range of temperatures, from the temperature minimum as represented by TRACE 1700 to the upper corona as represented by CDS Fe XVI. Oscillations are found to be present in all emission in this temperature range with frequencies in the range 5.4–8.9 mHz. We frequently find high frequency oscillations of $\sim$8.9 mHz in the data from the 26 Sep. Using the method of cross-spectral analysis time delays were found to be present between the different temperatures of emission suggesting the possibility of both upward and downward wave propagation. We suggest that the oscillations observed by us represent waves propagating up through the downflowing (redshifted) plasma in the sunspot umbral regions. It was found that there is a good correspondence between the oscillations in the low and high temperature regions even in locations where there is evidence for both upwardly and downwardly propagating waves (i.e. pixel 28B in Fig. 9). We suggest that this may be evidence for there being preferred frequencies of oscillation in the sunspot at which disturbances are constrained to oscillate. We present evidence that the downwardly propagating waves inferred by us may be the result of downwardly propagating magnetohydrodynamic waves from the corona. We found that a number of oscillation frequencies can exist co-spatially and simultaneously i.e. for one pixel three different frequencies at 5.40, 7.65 and 8.85 mHz were measured. The umbral oscillations are found to be present both in and outside of a sunspot plume, which indicates that oscillations are present in umbral regions irrespective of the presence of sunspot plumes. From a measurement of relative amplitudes we find that there is a tendency for the amplitudes to reach a maximum at the transition region temperature of O III (and less typically O V and Mg IX) and then to decrease to reach a minimum at the temperature of Mg X ($\log T = 6.0$ K), before increasing again at the temperature of Fe XVI. From a measurement of propagation speeds we suggest that the oscillations we observe are due to slow magnetoacoustic waves propagating up along the magnetic field lines.

Acknowledgements. We would like to thank the TRACE instrument team and the CDS and MDI instrument teams at Goddard Space Flight Centre for their help in obtaining the data. CDS and MDI are part of SOHO, the Solar and Heliospheric Observatory, which is a project of international cooperation between ESA and NASA. Original wavelet software was provided by C. Torrence and G. Compo, and is available at URL: `http://paos.colorado.edu/research/wavelets/`. This research was undertaken as part of the European Solar Magnetometry Network (ESMN) supported by the EU through the TMR programme (`http://www.phys.uu.nl/ rutten/tmr/`). We wish to thank Dr. Dipankar Banerjee and Dr. David Berghmans for helpful discussions.

References

Andretta, V., & Jones, H. P. 1997, ApJ, 489, 375
Banerjee, D., O'Shea, E., Goossens, M., & Doyle, J. G. 2002, A&A, in preparation
Brynildsen, N., Leifsen, T., Kjeldseth-Moe, O., Maltby, P., & Wilhelm, K. 1999a, ApJ, 511, L121
Brynildsen, N., Kjeldseth-Moe, O., Maltby, P., & Wilhelm, K. 1999b, ApJ, 517, L159
Brynildsen, N., Maltby, P., Brekke, P., Haugan, S. V. H., & Kjeldseth-Moe, O. 1999c, Sol. Phys., 186, 141
Brynildsen, N., Maltby, P., Leifsen, T., Kjeldseth-Moe, O., & Wilhelm, K. 2000, Sol. Phys., 191, 129
Brynildsen, N., Maltby, P., Fredvik, T., Kjeldseth-Moe, O., & Wilhelm, K. 2001, Sol. Phys., 198, 89
Carlsson, M., & Stein, R. F. 1997, ApJ, 481, 500
Doyle, J. G., Raymond, J. C., Noyes, R. W., & Kingston, A. E. 1985, ApJ, 297, 816
Doyle, J. G., van den Oord, G. H. J., O'Shea, E., & Banerjee, D. 1998, Sol. Phys., 181, 51
Doyle, J. G., van den Oord, G. H. J., O'Shea, E., & Banerjee, D. 1999, A&A, 347, 335
Fludra, A. 1999, A&A, 344, L75
Fludra, A. 2001, A&A, 368, 639
Gurman, J. B., Leibacher, J. W., Shine, R. A., Woodgate, B. E., & Henze, W. 1982, ApJ, 253, 939
Gurman, J. B., & Leibacher, J. W. 1984, ApJ, 283, 859
Handy, B. N., Acton, L. W., Kankelborg, C. C., et al. 1999, Sol. Phys., 187, 229
Hansteen, V. 1997, Proc. of the fifth SOHO workshop: The corona and solar wind near minimum activity, ESA-SP 404, 45
Harrison, R. A., Sawyer, E. C., Carter, M. K., et al. 1995, Sol. Phys., 162, 233
Judge, P. G., Tarbell, T. D., & Wilhelm, K. 2001, ApJ, 554, 424
Lites, B. W. 1986a, ApJ, 301, 992
Lites, B. W., 1986b, ApJ, 301, 1005
Lites, B. W. 1992, in Sunspots: Theory and Observations, ed. J. H. Thomas, & N. O. Weiss (Kluwer Academic Publishers, Dordrecht), 261
Maltby, P., Brynildsen, N., Fredvik, T., Kjeldseth-Moe, O., & Wilhelm, K. 1999, Sol. Phys., 190, 437
Maltby, P., Brynildsen, N., Kjeldseth-Moe, O., & Wilhelm, K. 2001, A&A, 373, L1
Mazzotta, P., Mazzitelli, G., Colafrancesco, S., & Vittorio, N. 1998, A&AS, 133, 403
Muglach, K. 2002, A&A, in preparation
Obridko, V. N., & Staude, J. 1988, A&A, 189, 232
O'Shea, E., Banerjee, D., Doyle, J. G., Fleck, B., & Murtagh, F. 2001, A&A, 368, 1095
Pérez, M. E., Doyle, J. G., O'Shea, E., & Keenan, F. P. 1999, A&A, 351, 1139
Scherrer, P. H., Bogart, R. S., Bush, R. I., et al. 1995, Sol. Phys., 162, 129
Thomas, J. H., & Scheuer, M. A. 1982, Sol. Phys., 79, 19
Thomas, J. H. 1984, A&A, 135, 188
Thomas, J. H., Lites, B. W., Gurman, J. B., & Ladd, E. F. 1987, ApJ, 312, 457
Thomas, J. H., & Weiss, N. O. 1992, in Sunspots: Theory and Observations, ed. J. H. Thomas, & N. O. Weiss (Kluwer Academic Publishers, Dordrecht), 3
Torrence, C., & Compo, G. P. 1998, Bull. Amer. Meteor. Soc., 79, 61
Vernazza, J. E., Avrett, E. H., & Loeser, R. 1981, ApJS, 45, 635
Žugžda, Y. D., Staude, J., & Locans, V. 1984, Sol. Phys., 91, 219